Revealing Insight into Defect-Mediated Charge Dynamics and Reaction Intermediates Stabilization for CO_2 Photoreduction on S-scheme Catalyst

Muhammad Rizwan Kamal[a,b], Shu-Long Li[c], Hongyuan Zhou[c], Bo Wang[d], Wenxuan Chu[b], Chuan Ke[e], Min Liu[f], Li Zhong[f], Jiabao Yi[g], Lin Xu[h*], Zhenghua Wu[h*], Sharafat Ali[c], Mohammad Z. Rahman[c*], Liang Qiao[b*]

[a]School of Intelligent Manufacturing, Qingdao Hengxing University of Science and Technology, Qingdao 266100, China

[b]School of Physics, University of Electronic Science and Technology of China, Chengdu 610054, China

[c]Institute for Advanced Study, Chengdu University, Chengdu 610106, China

[d]College of Chemical and Biological Engineering, Shandong University of Science and Technology, Qingdao, Shandong Province 266590, China

[e]Center for Quantum Materials and Devices, School of Intelligent Manufacturing, Sichuan University of Arts and Science, Dazhou 635000, China

[f]SEU-FEI Nano-Pico Center, Key Laboratory of MEMS of Ministry of Education, Southeast University, Nanjing 210096, China

[g]Department of Chemical Engineering and Interdisciplinary Research Center for Hydrogen Technologies and Carbon Management (IRC-HTCM), King Fahd University of Petroleum and Minerals, 31261 Dhahran, Saudi Arabia

[h]School of Electronic Science and Engineering, University of Electronic Science and Technology of China, Chengdu 611731, China

Corresponding authors e-mail: xulin@uestc.edu.cn; wuzhenhua@uestc.edu.cn; mohammadziaurrahman@cdu.edu.cn; liang.qiao@uestc.edu.cn

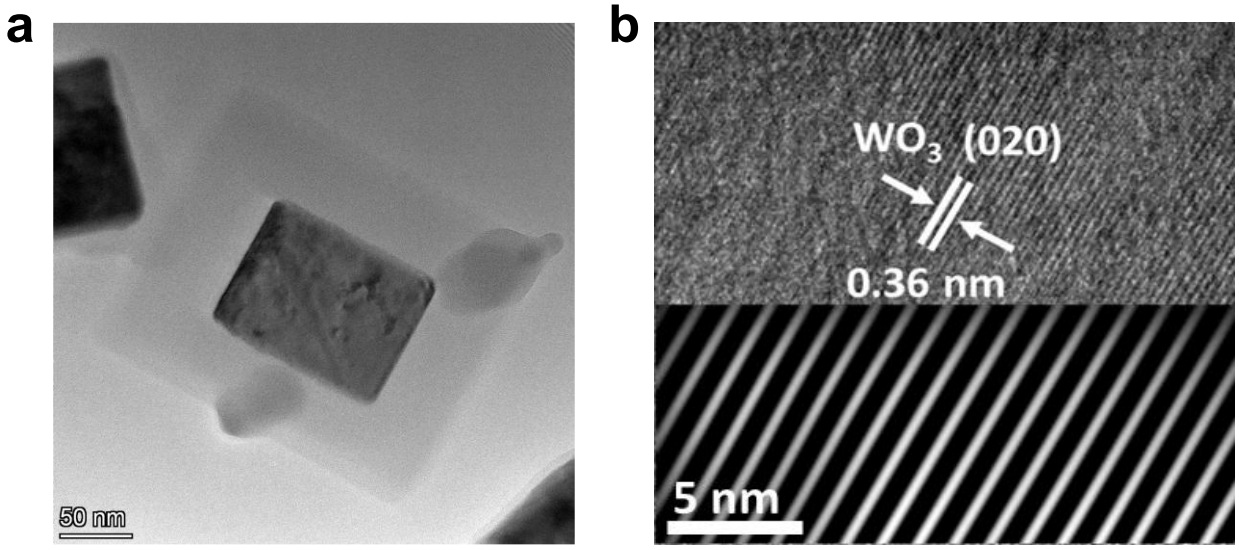

Figure S1. (a) The TEM and (b) HRTEM (IFFT inset) image of Bulk WO_3.

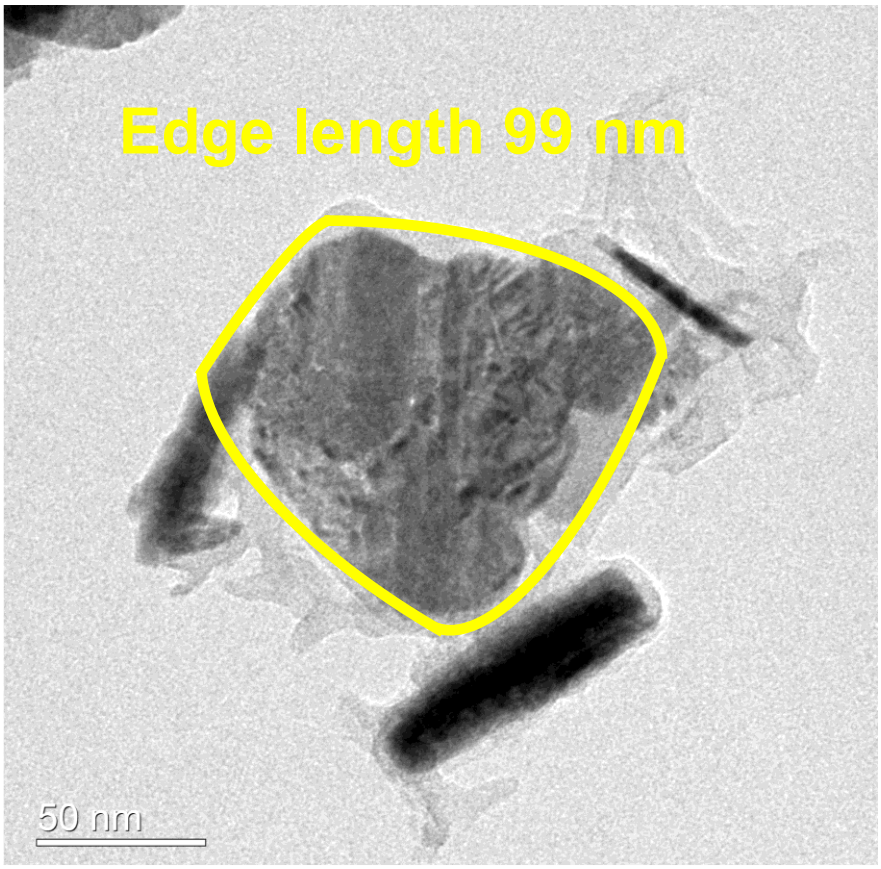

Figure S2. The average edge length of CW.

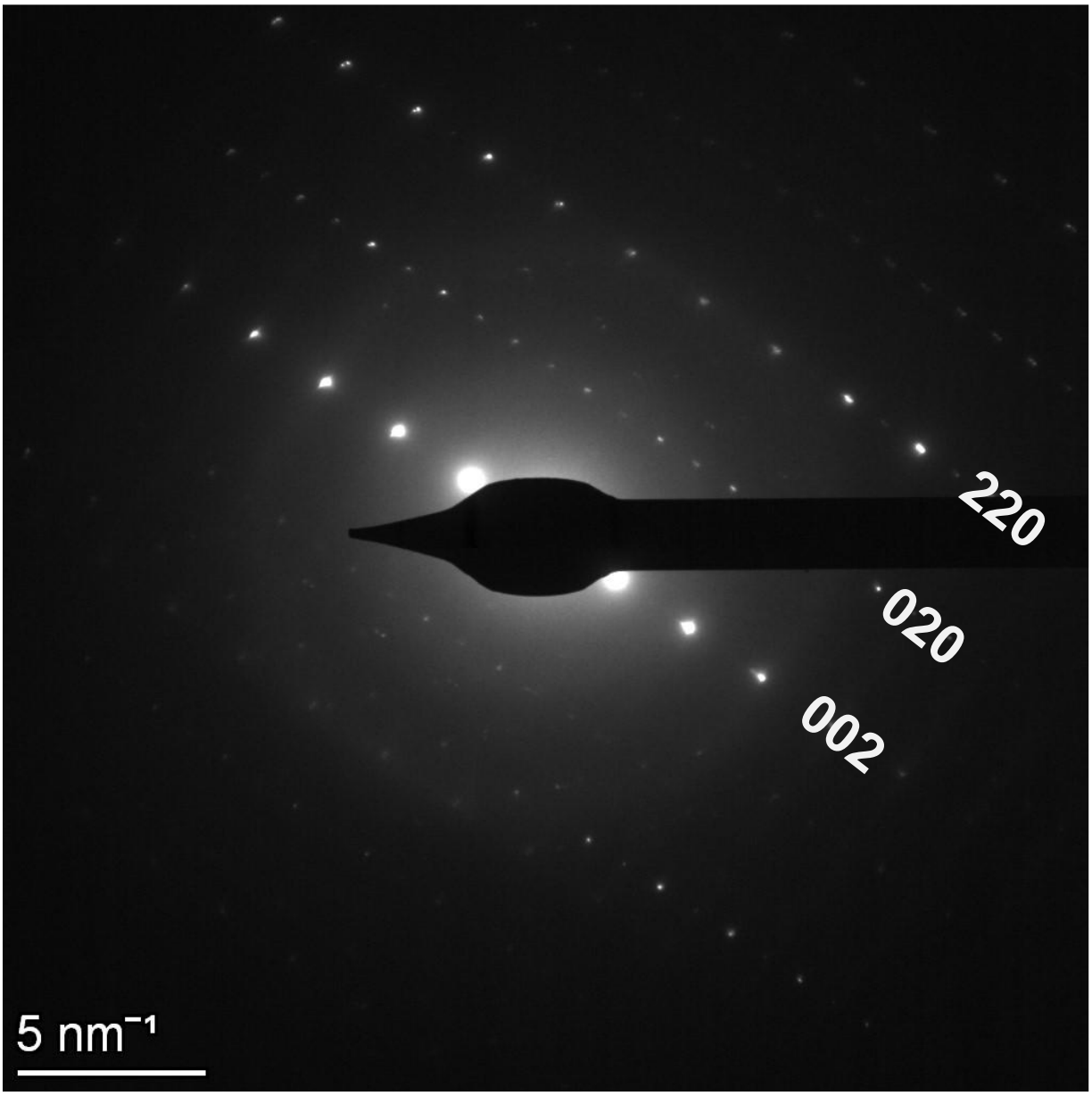

Figure S3. SAED pattern of Bulk WO_3.

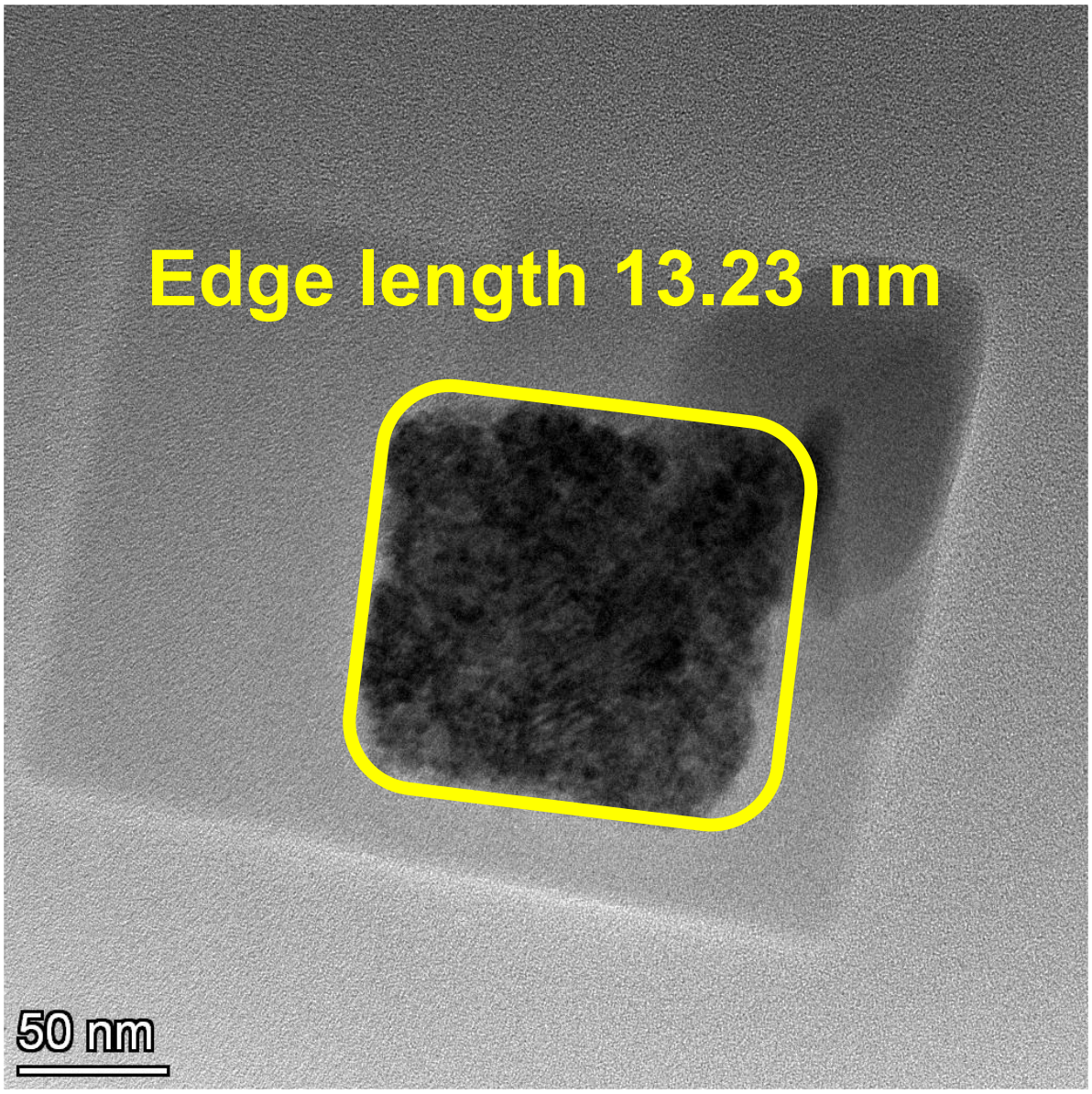

Figure S4. The average edge length of CTS/rGO/CW.

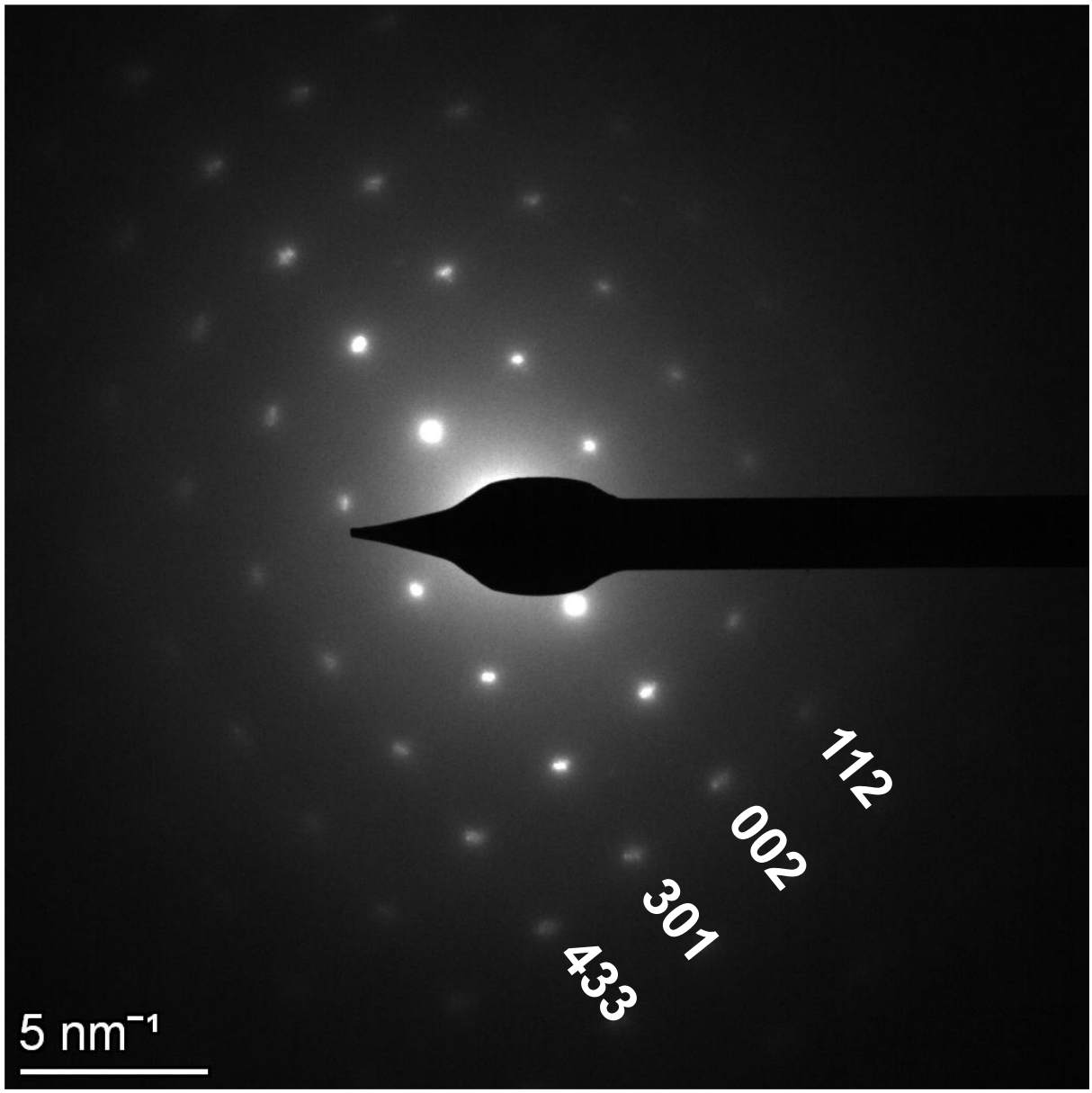

Figure S5. SAED pattern of CTS/rGO/CW.

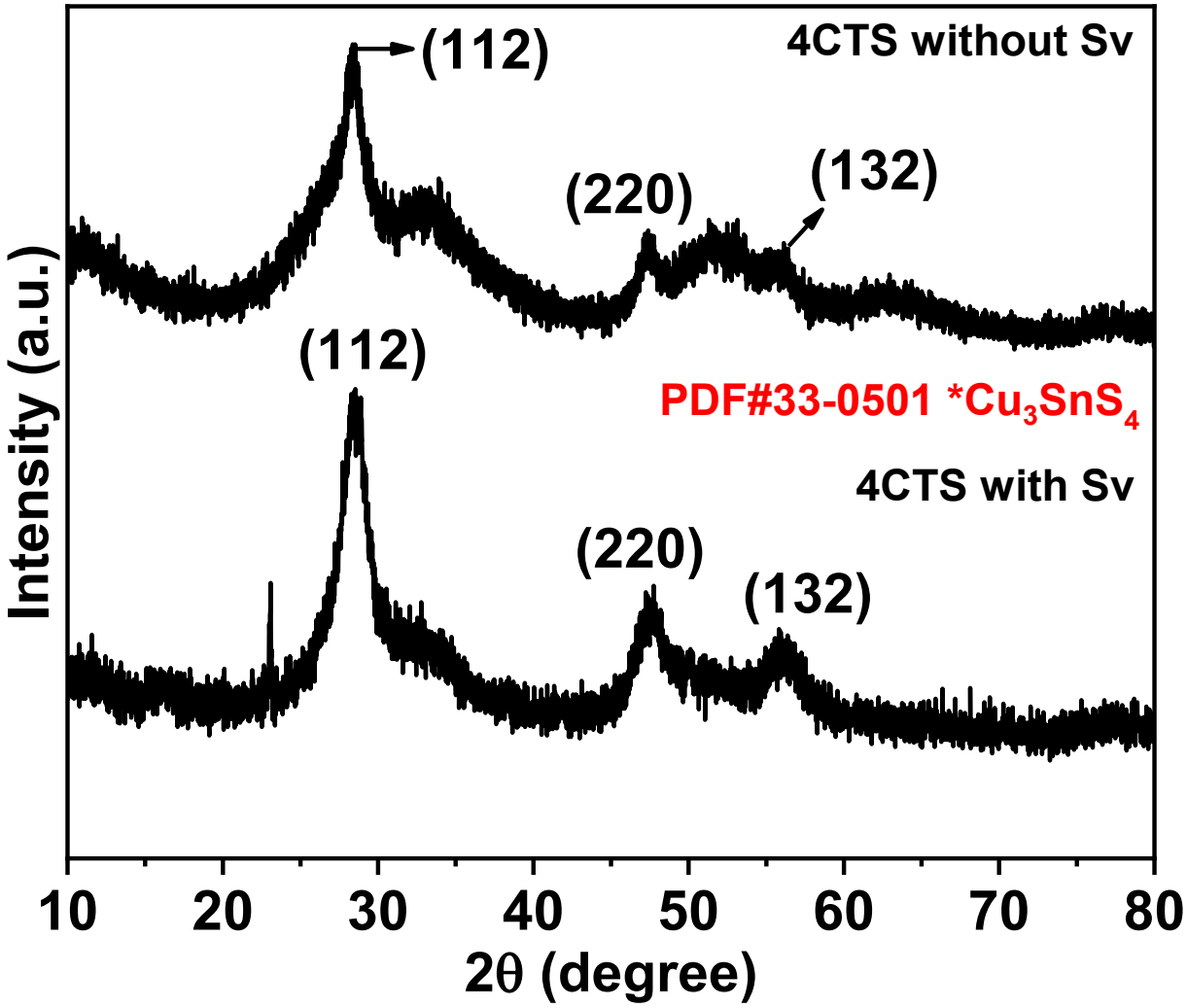

Figure S6. XRD pattern of 4CTS with and without S vacancy.

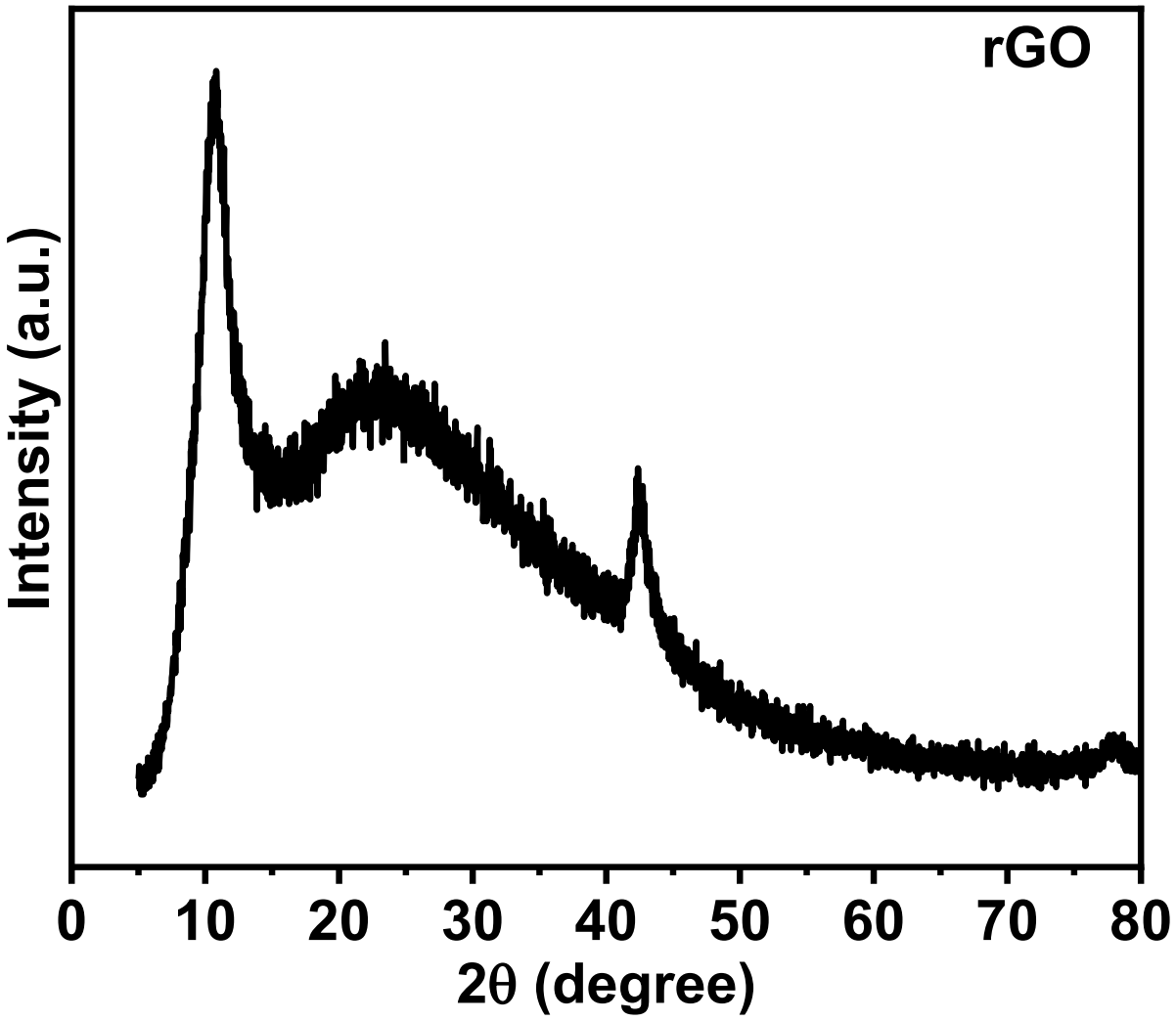

Figure S7. XRD pattern of rGO.

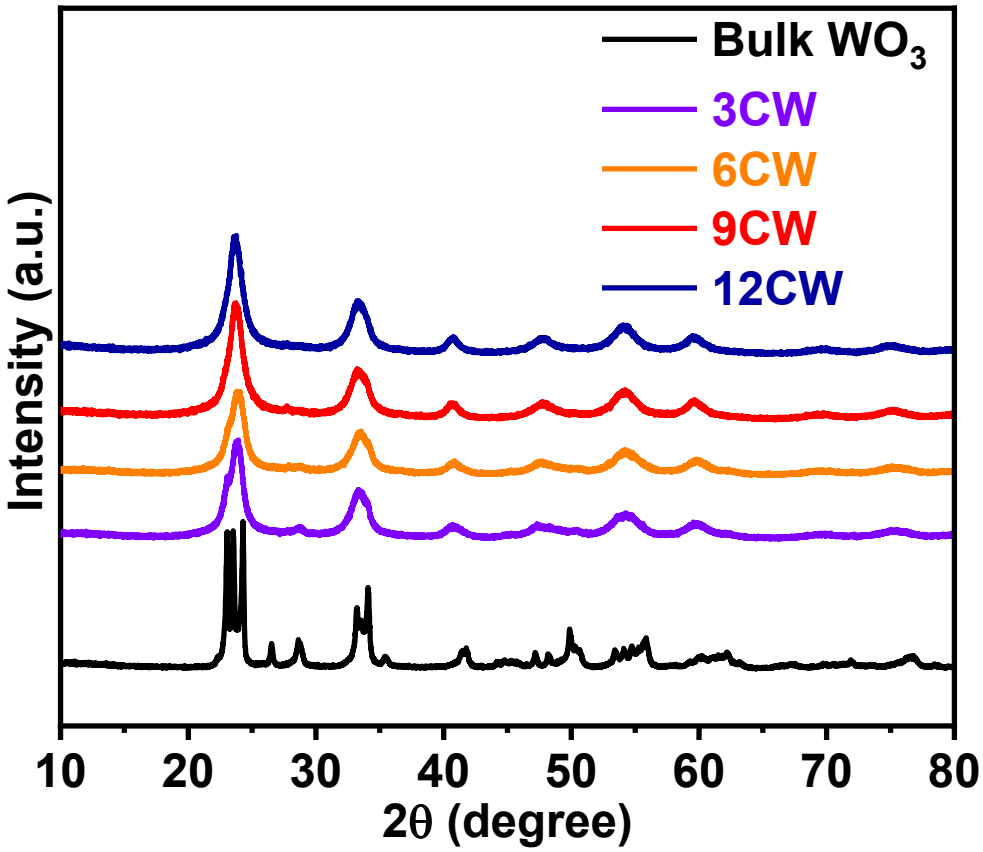

Figure S8. XRD pattern of Bulk WO_3 and zCW.

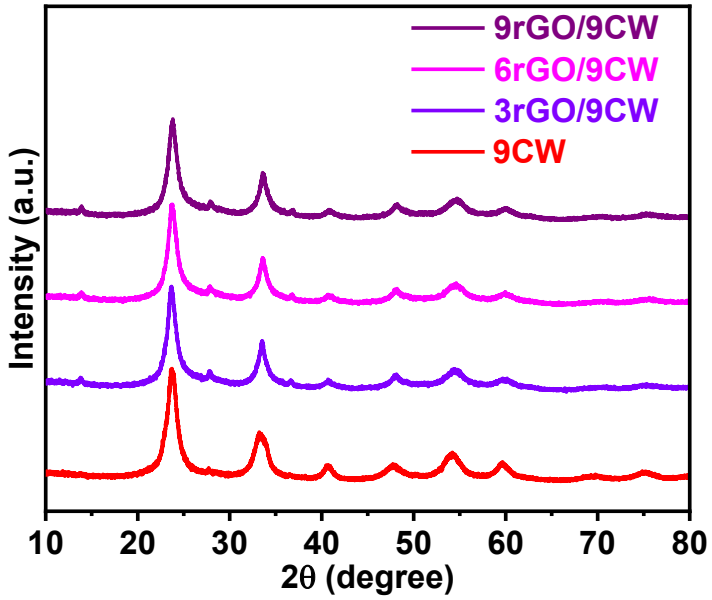

Figure S9. XRD pattern of 9CW and yrGO/9CW.

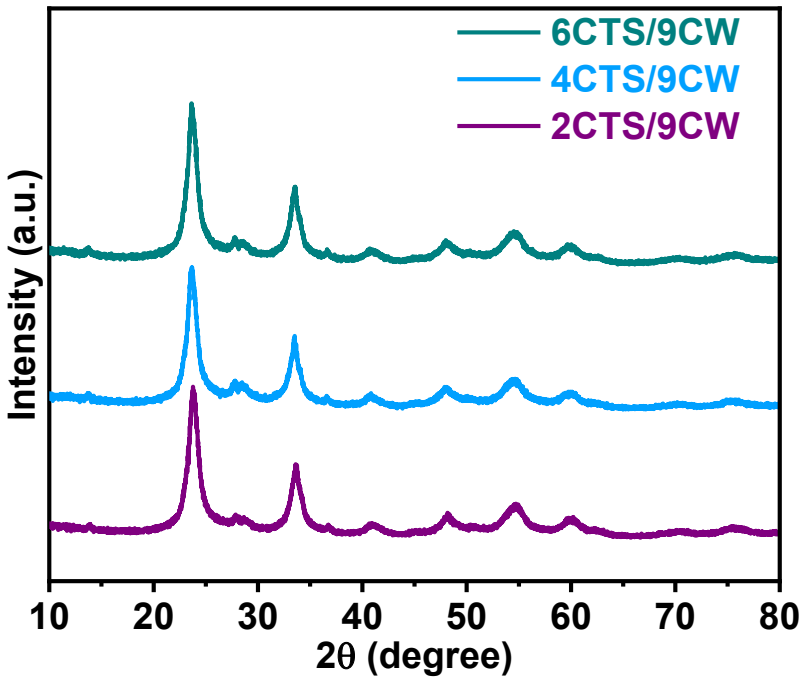

Figure S10. XRD pattern of xCTS/9CW.

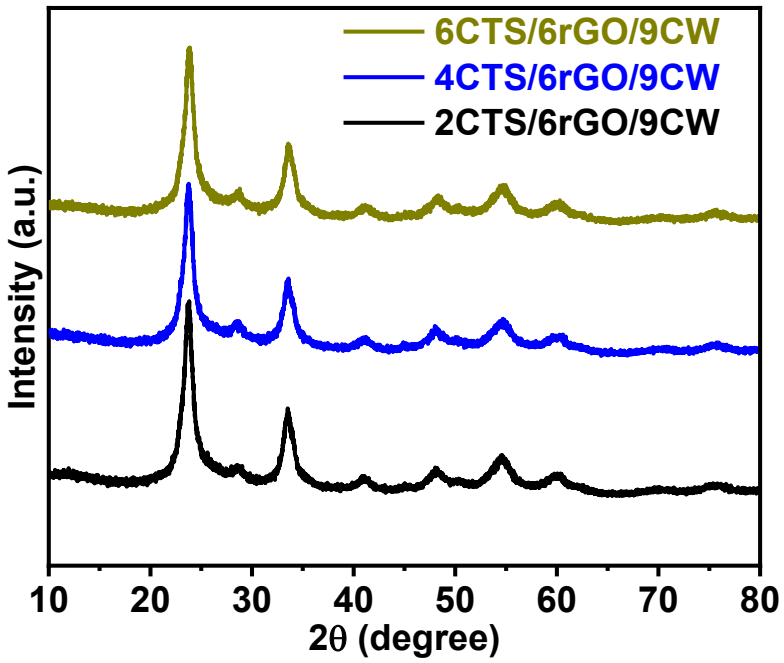

Figure S11. XRD pattern of xCTS/6rGO/9CW.

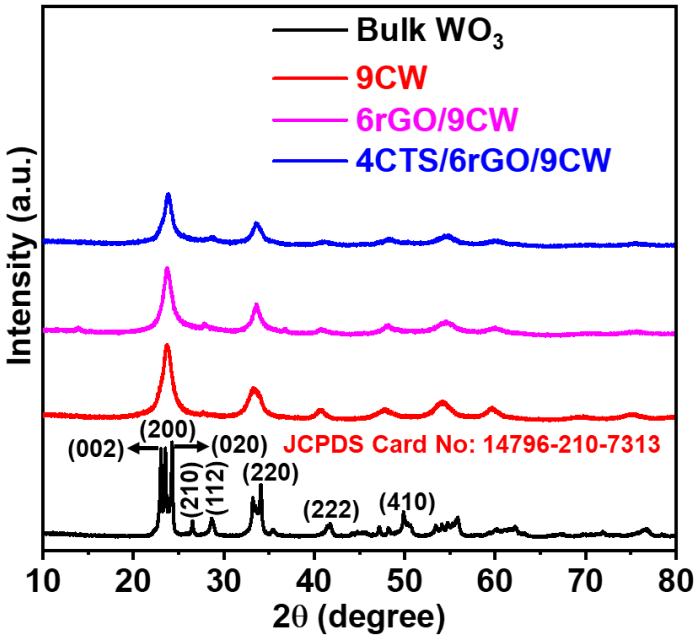

Figure S12. XRD pattern of Bulk WO_3, 9CW, 6rGO/9CW, and 4CTS/6rGO/9CW.

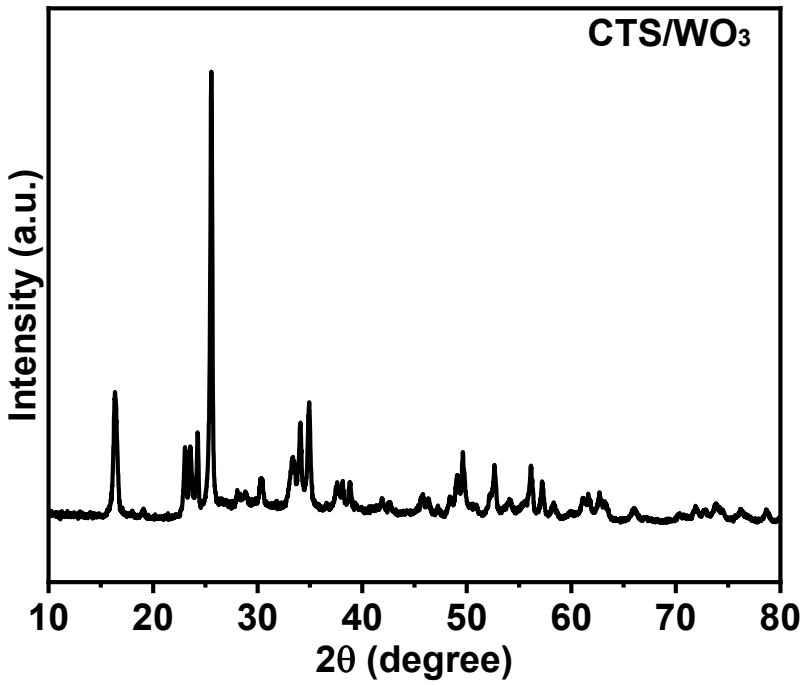

Figure S13. XRD pattern of CTS/WO_3 without S and O vacancy.

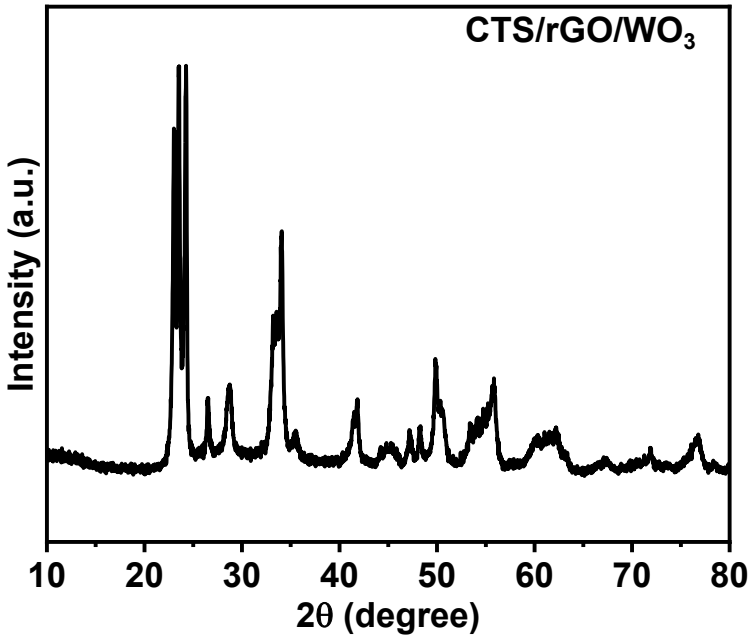

Figure S14. XRD pattern of CTS/rGO/WO_3 without S and O vacancy.

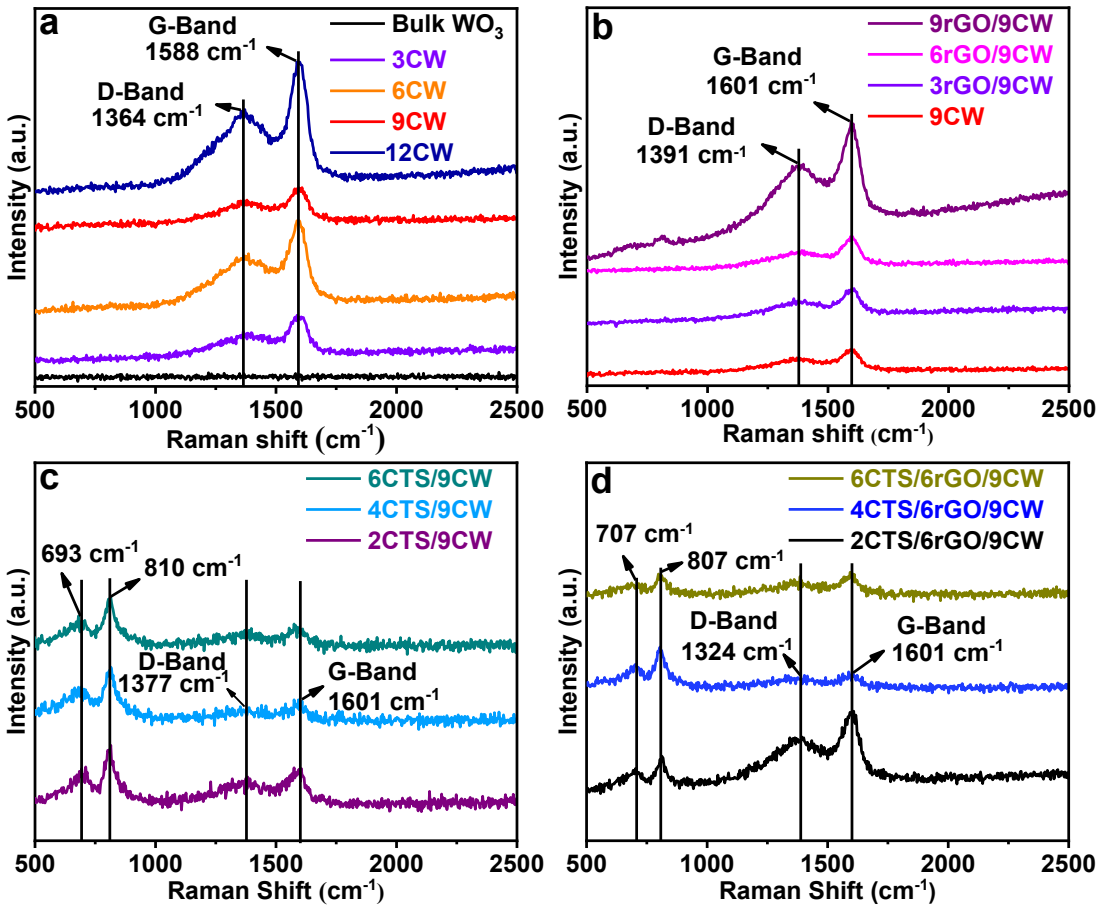

Figure S15. Raman spectra of (a) Bulk WO_3 and zCW, (b) 9CW and yrGO/9CW, (c) xCTS/9CW, and (d) zCTS/6rGO/9CW (z=2, 4 and 6).

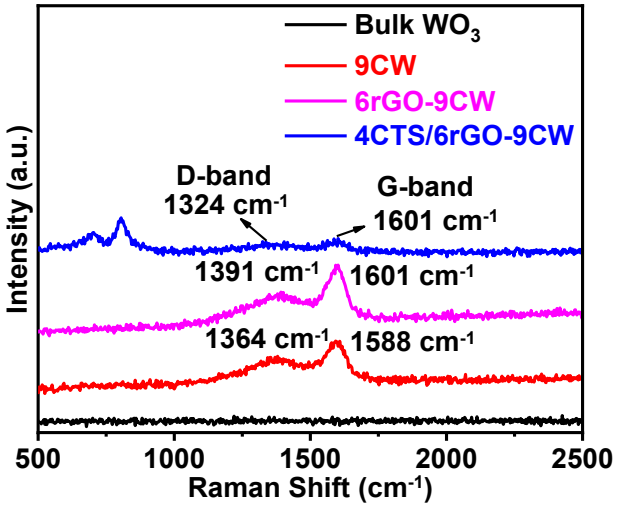

Figure S16. Raman spectra of Bulk WO_3, 9CW, 6rGO/9CW, and 4CTS/6rGO/9CW.

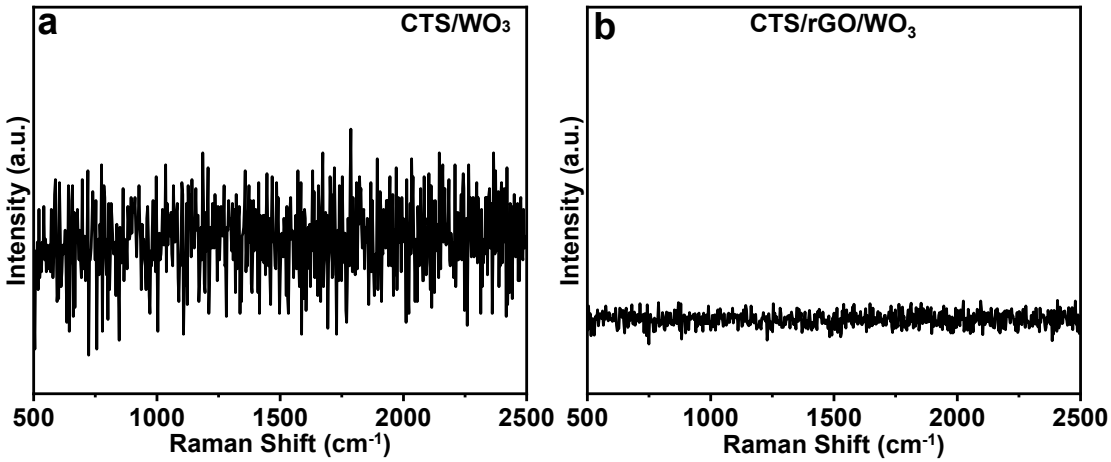

Figure S17. Raman spectra of (a) CTS/WO_3 and (b) (CTS/rGO/WO_3) without S and O vacancy.

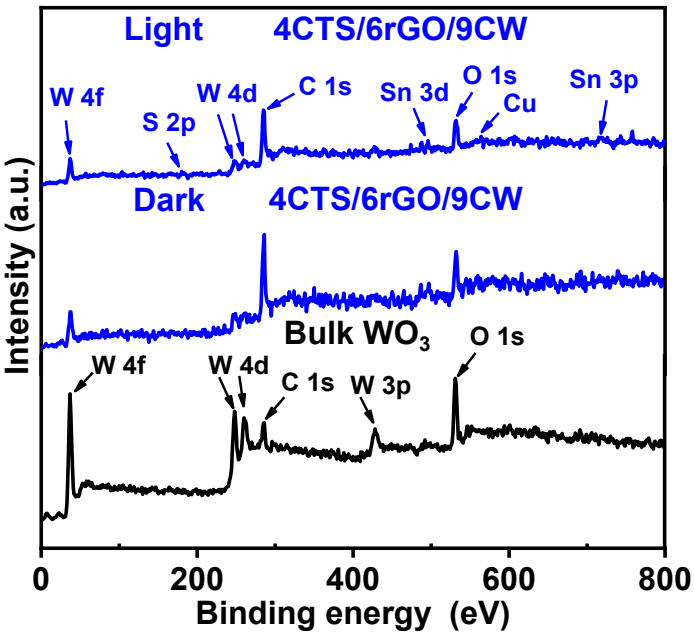

Figure S18. XPS survey spectra of Bulk WO_3, and 4CTS/6rGO/9CW heterojunction in dark and light.

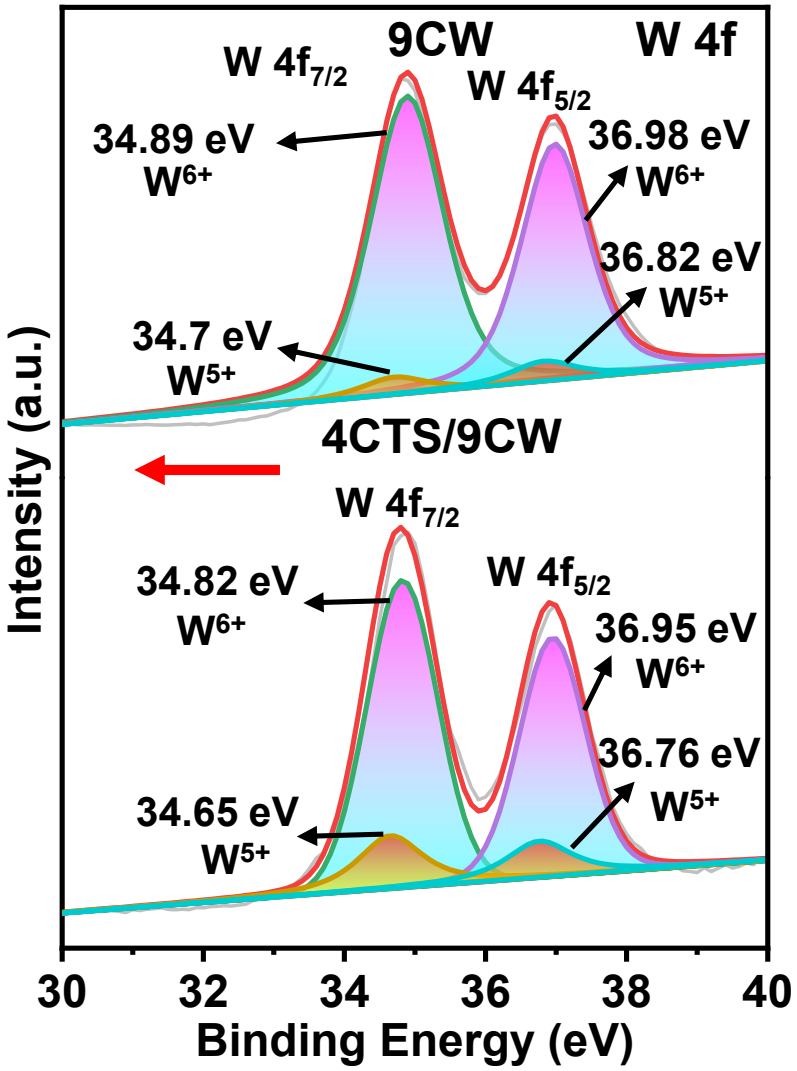

Figure S19. XPS spectra of W 4f for 9CW and 4CTS/9CW.

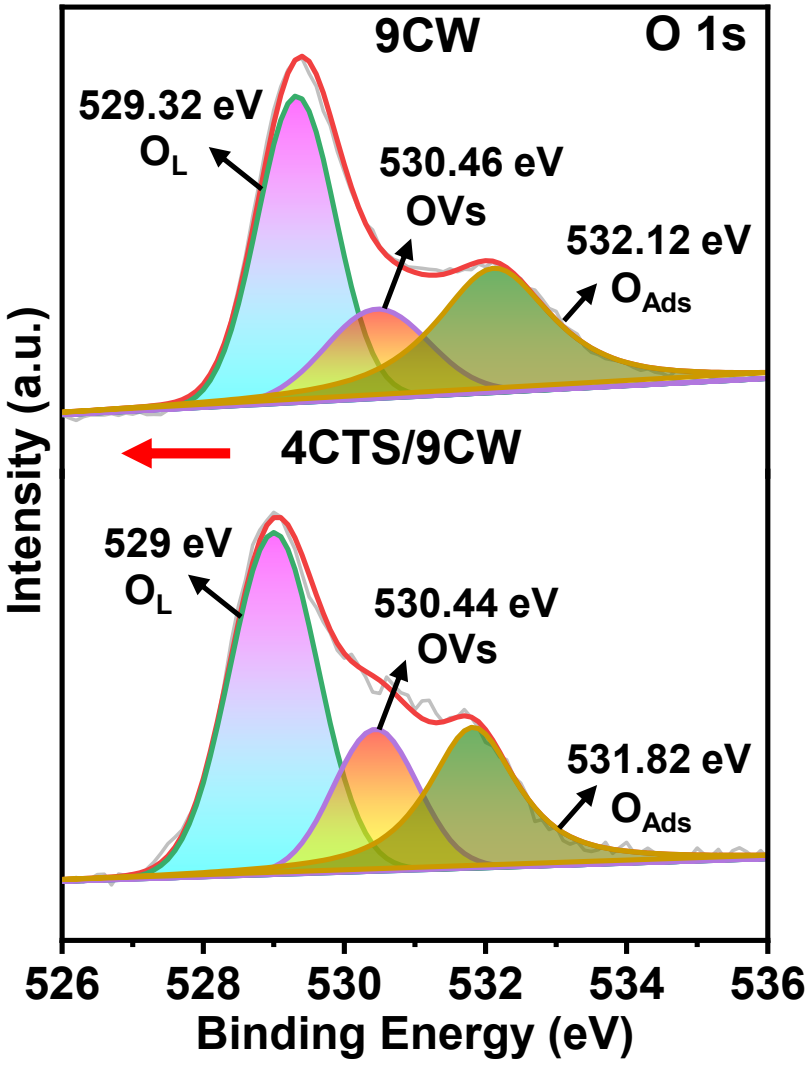

Figure S20. XPS spectra of O 1s for 9CW and 4CTS/9CW.

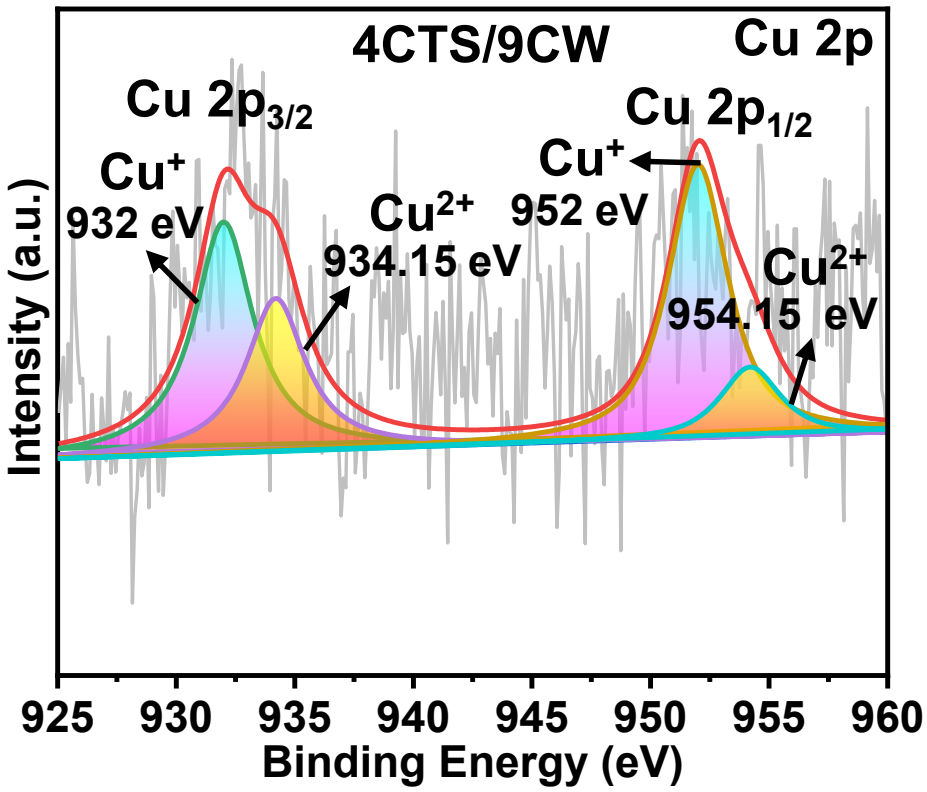

Figure S21. XPS spectra of Cu 2p for 4CTS/9CW.

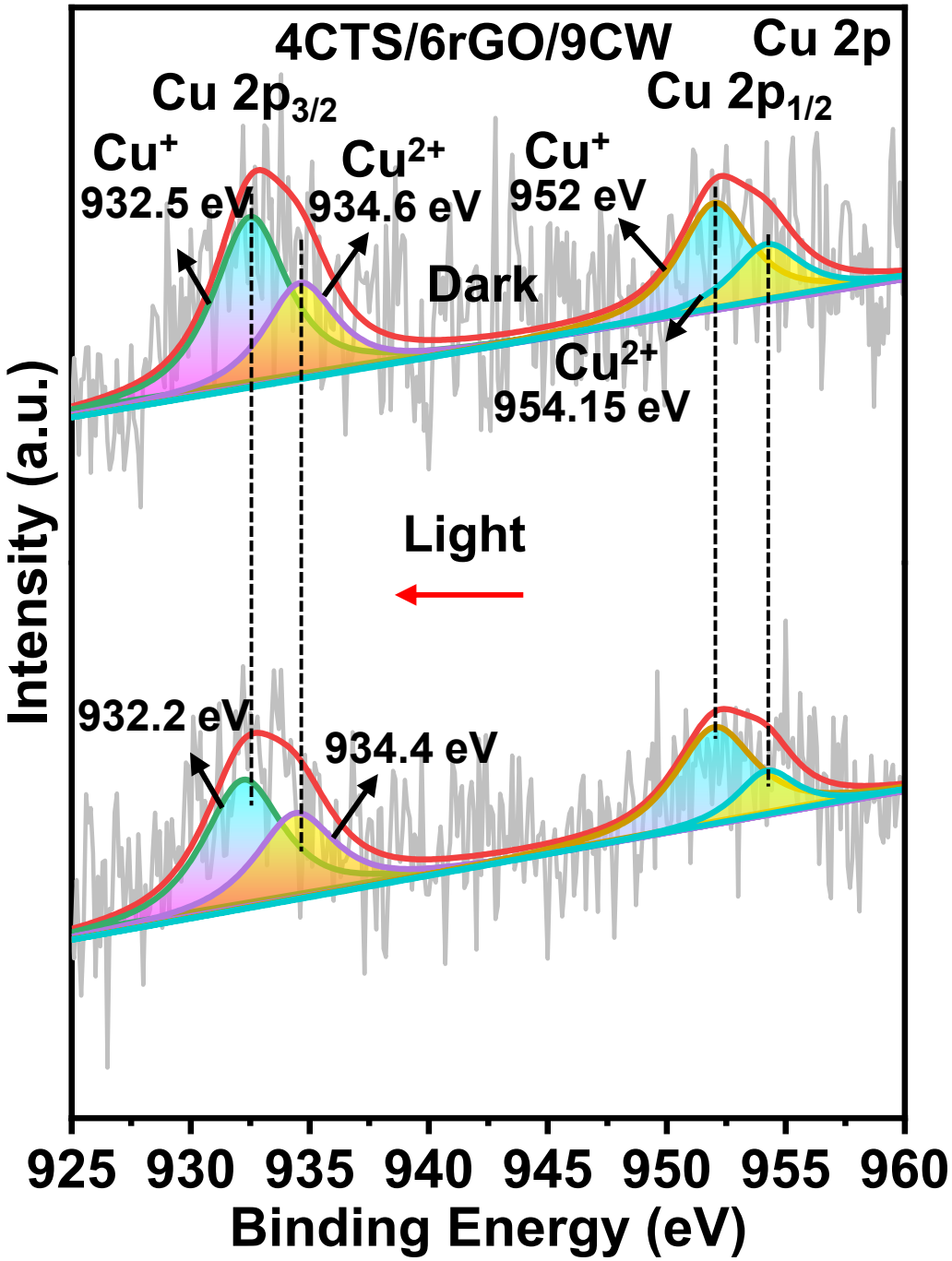

Figure S22. XPS spectra of Cu 2p for 4CTS/6rGO/9CW in dark and light.

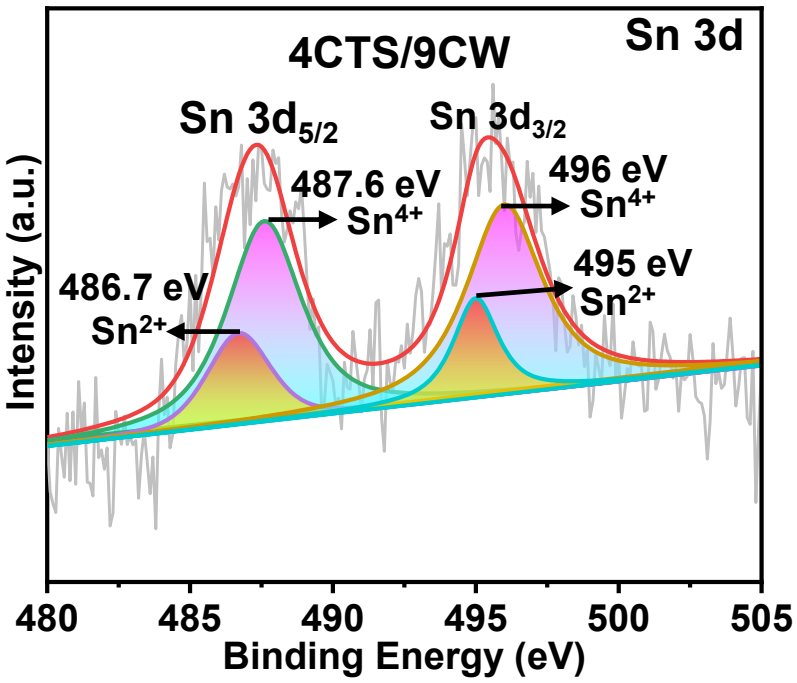

Figure S23. XPS spectra of Sn 3d for 4CTS/9CW.

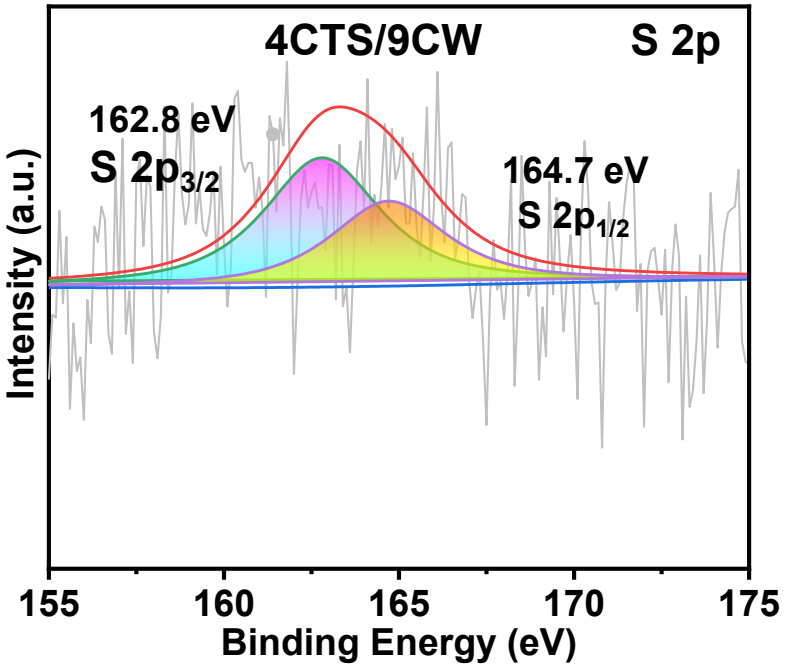

Figure S24. XPS spectra of S 2p for 4CTS/9CW.

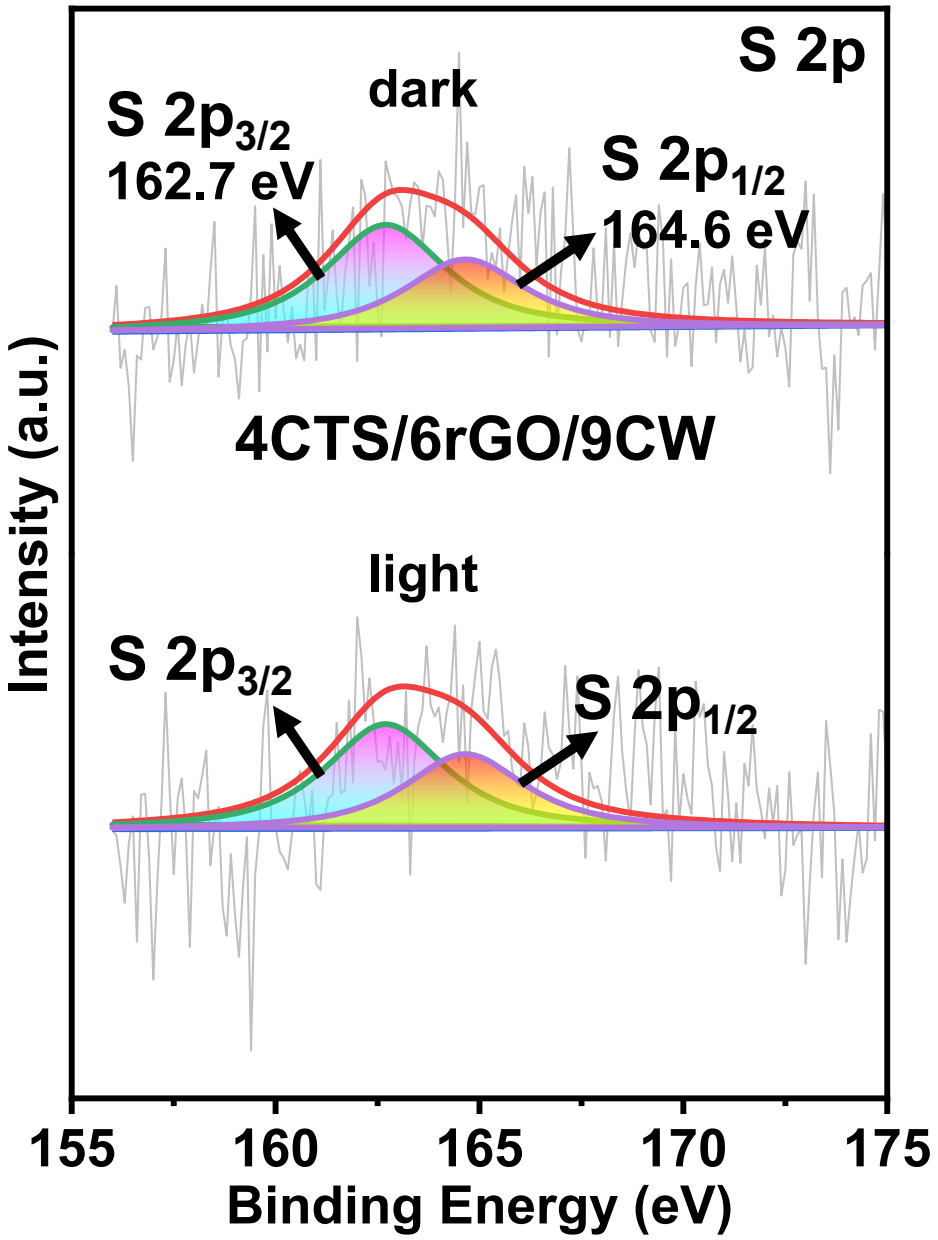

Figure S25. XPS spectra of S 2p for 4CTS/6rGO/9CW heterojunction in dark and light.

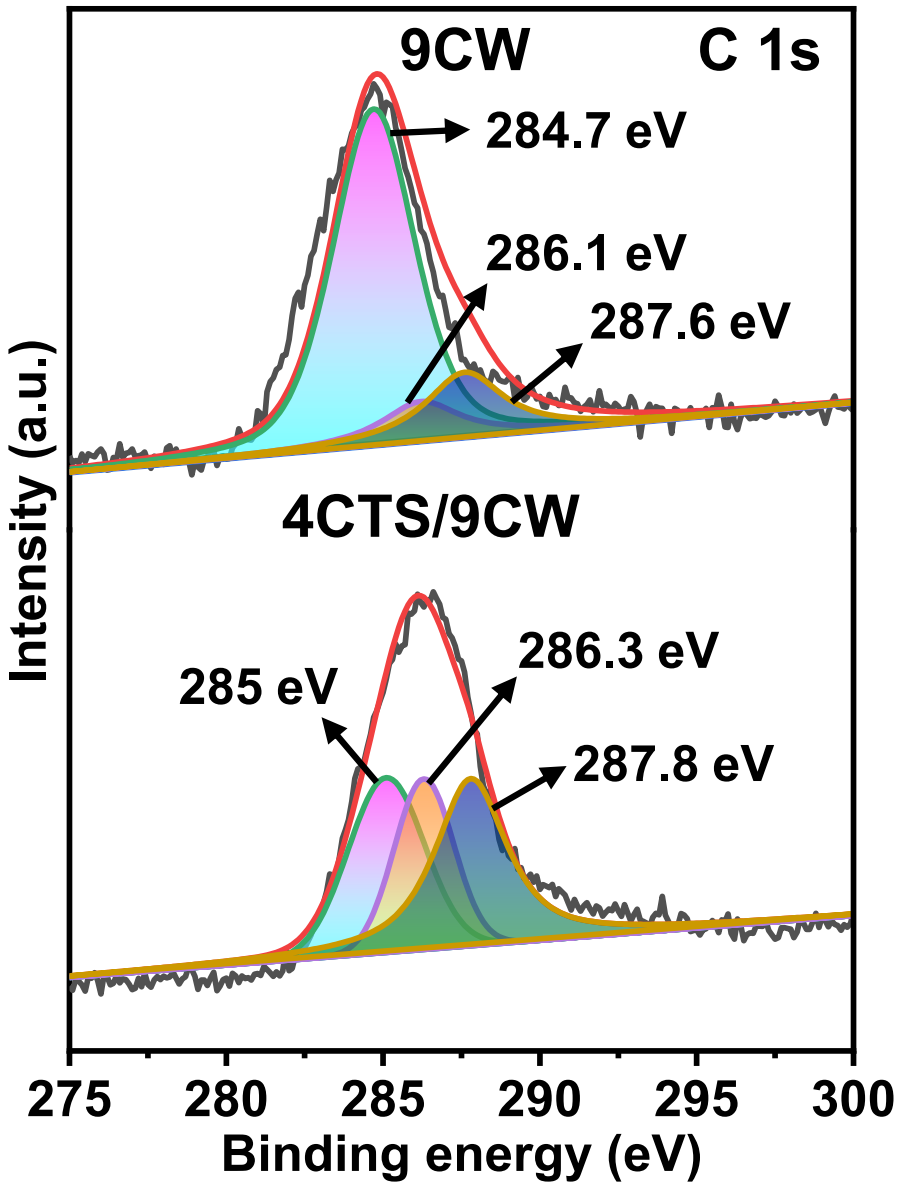

Figure S26. XPS spectra of C 1s for 9CW and 4CTS/9CW.

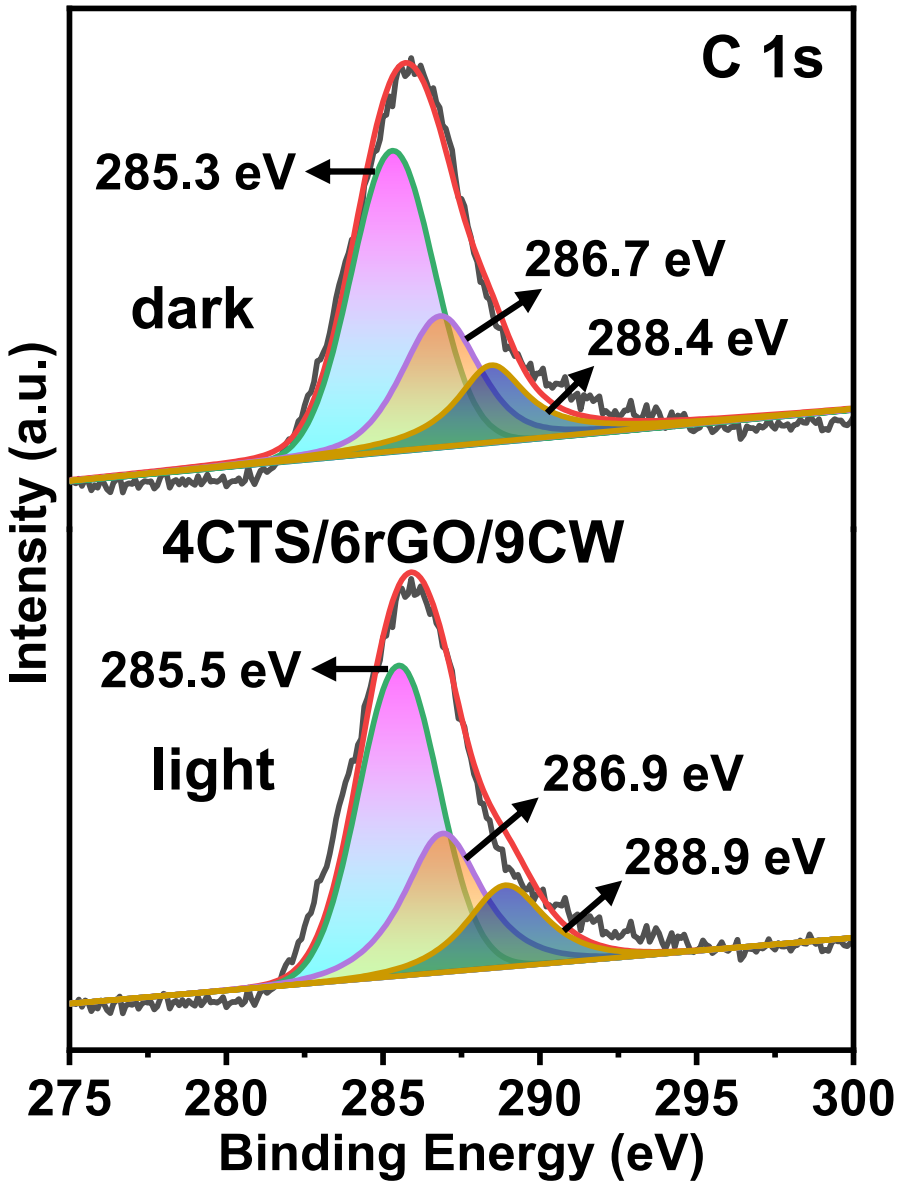

Figure S27. XPS spectra of C 1s for 4CTS/6rGO/9CW in dark and light.

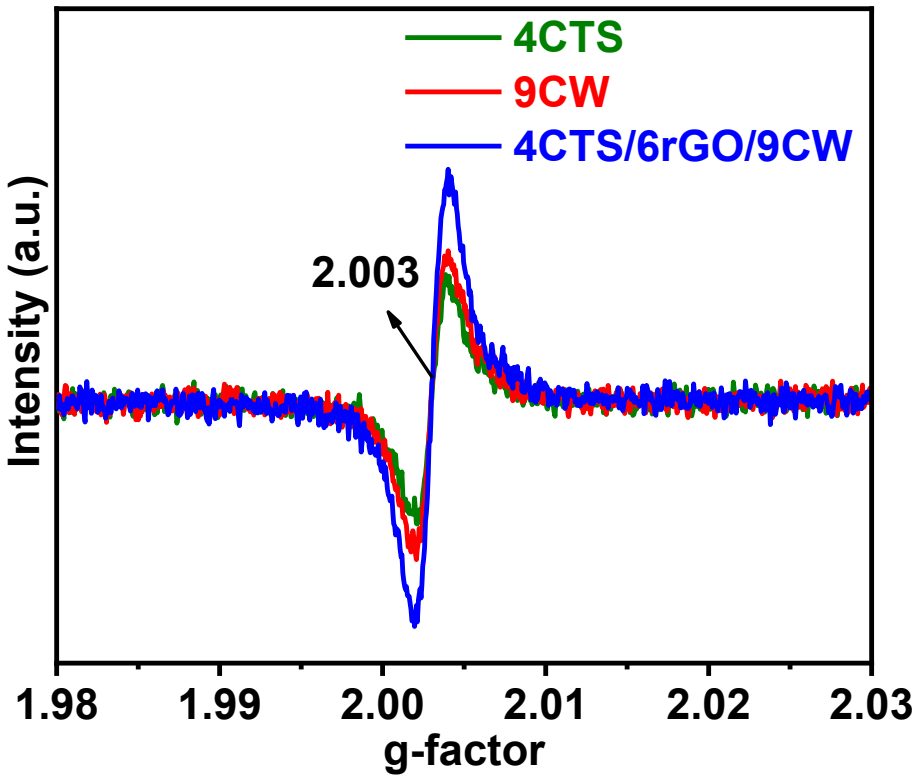

Figure S28. g-factor value of 9CW, 4CTS, and 4CTS/6rGO/9CW.

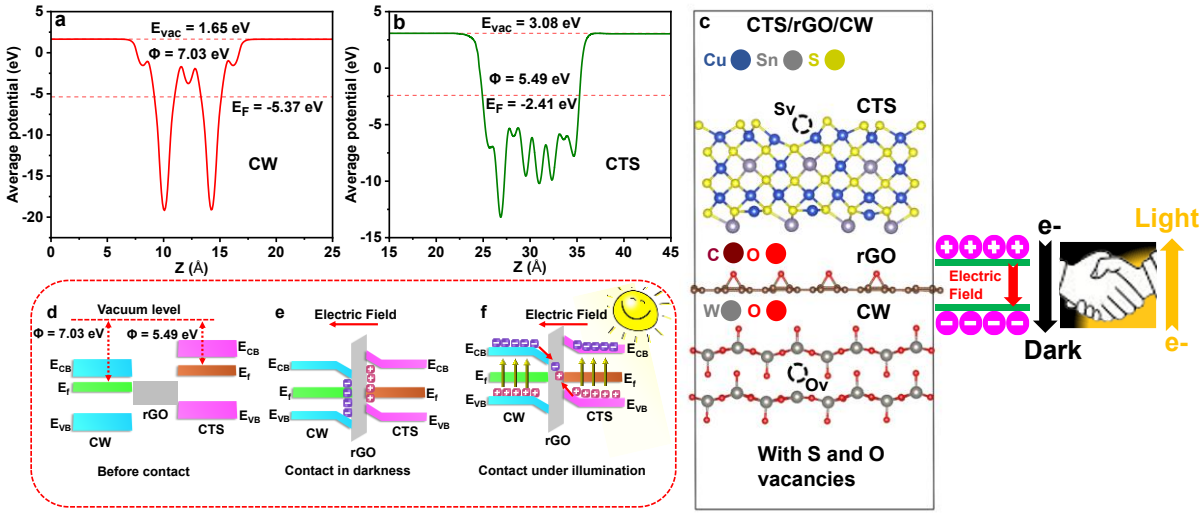

Figure S29. DFT calculated work function for (a) CW, (b) CTS, (c) DFT electronic structure of dual S/O vacancy-rich CTS/rGO/CW heterojunction, (d) CTS/rGO/CW S-scheme heterojunction before contact (e) after contact, and (f) under illumination.

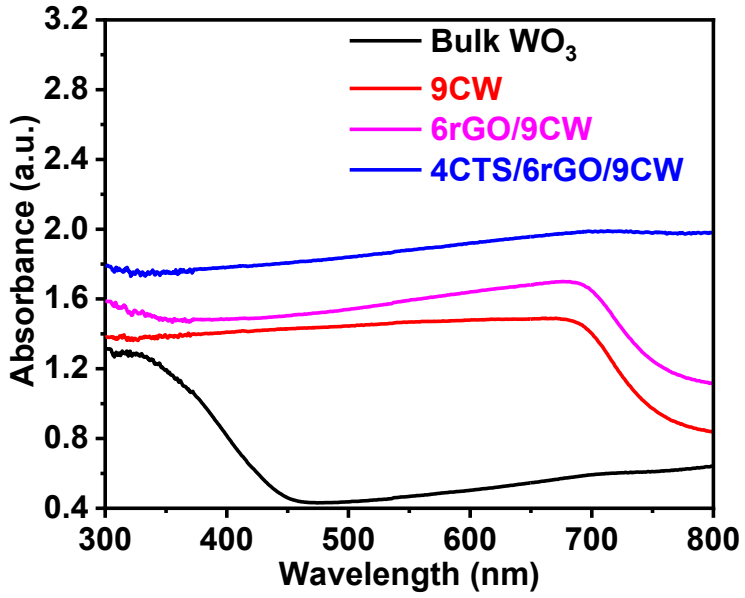

Figure S30. UV-vis diffuse reflectance spectra of bulk WO_3, 9CW, 6rGO/9CW, and 4CTS/6rGO/9CW.

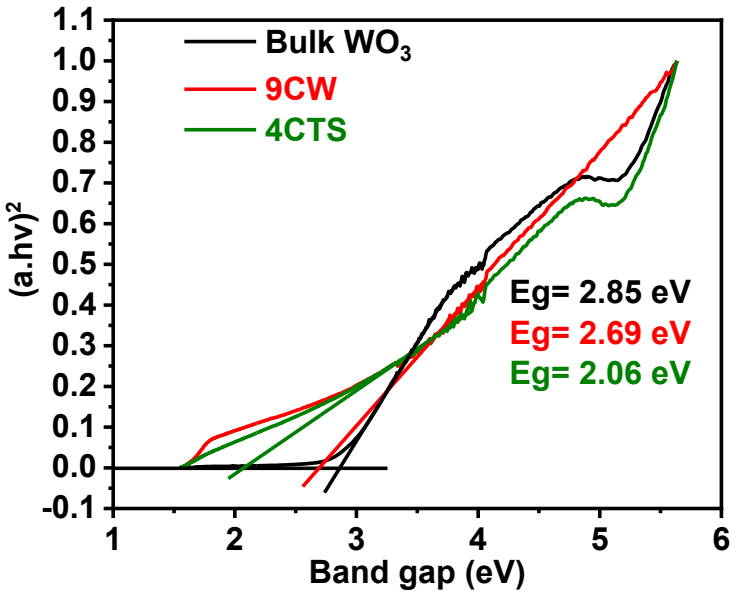

Figure S31. Tauc plots of Bulk WO_3, 9CW, and 4CTS.

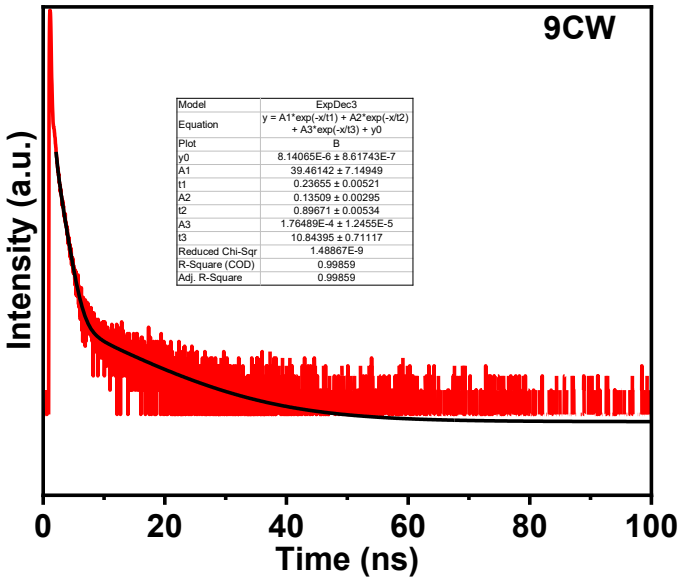

Figure S32. TRPL decay curve and fitting with tri-exponential model for 9CW.

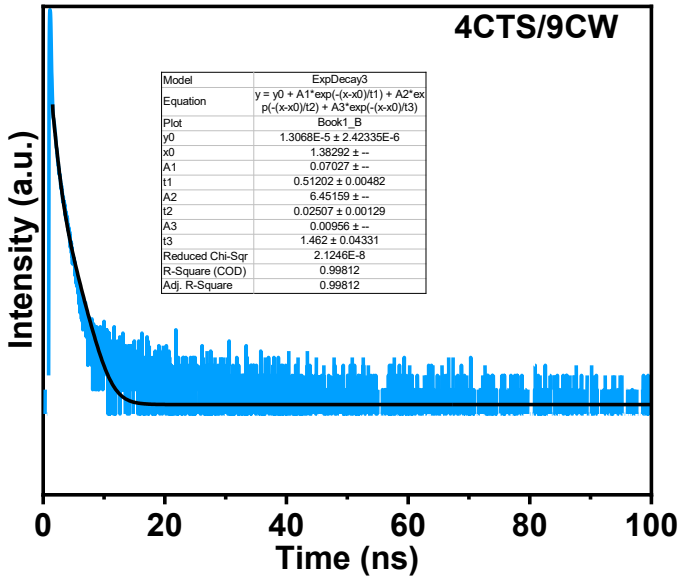

Figure S33. TRPL decay curve and fitting with tri-exponential model for 4CTS/9CW.

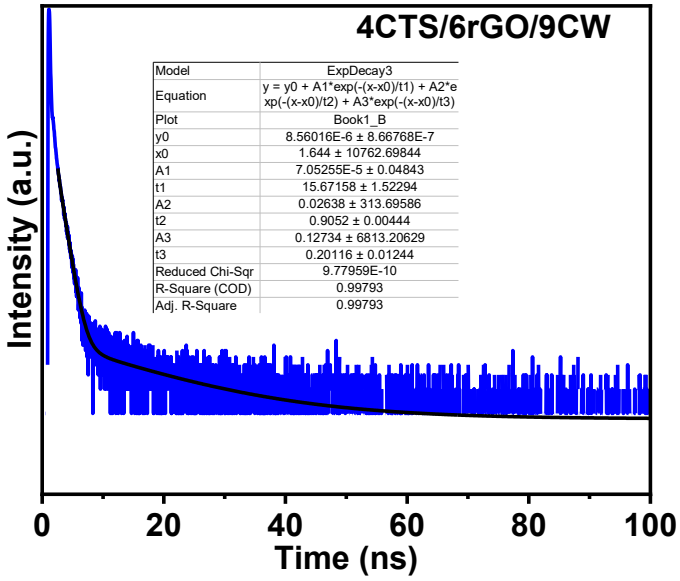

Figure S34. TRPL decay curve and fitting with tri-exponential model for 4CTS/6rGO/9CW.

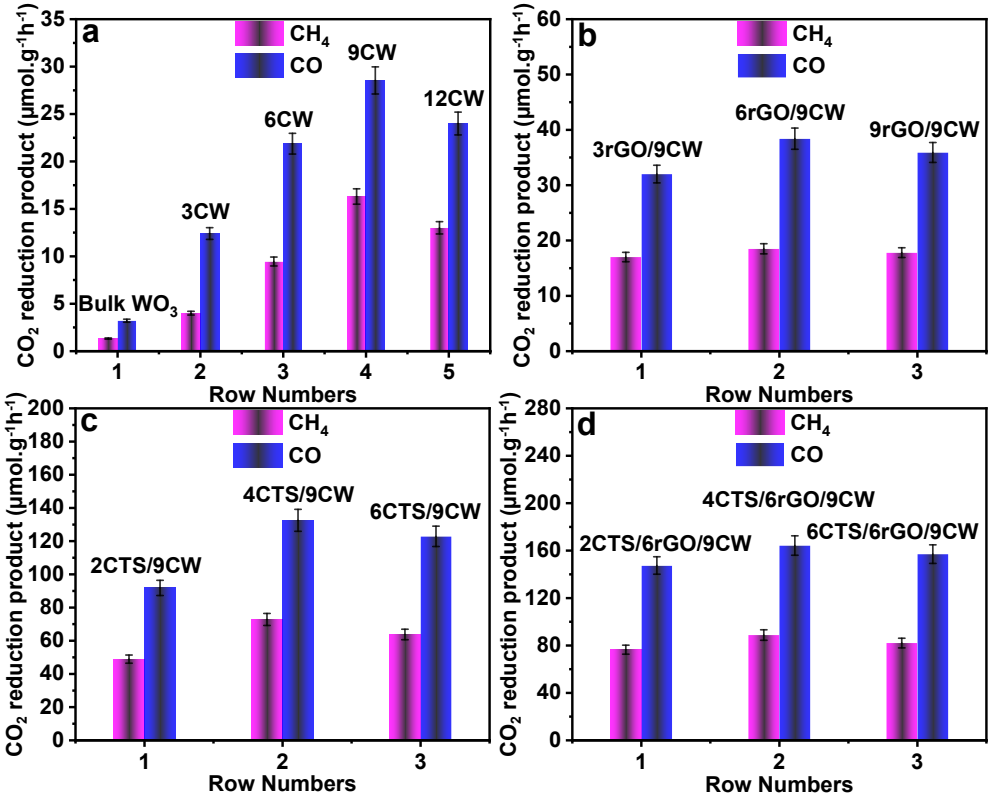

Figure S35. Photocatalytic activity of (a) Bulk WO_3 and zCW, (b) yrGO/9CW, (c) xCTS/9CW, (d) xCTS/6rGO/9CW.

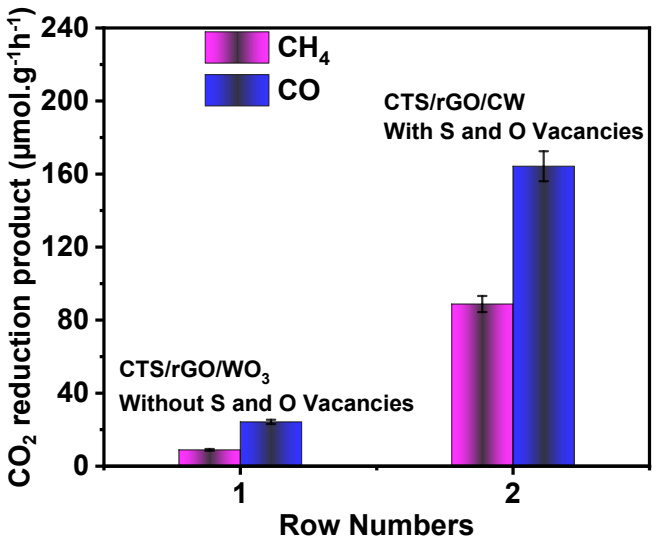

Figure S36. Photocatalytic CO_2 reduction performance comparison between CTS/rGO/WO_3 without S and O vacancies and CTS/rGO/CW with vacancies.

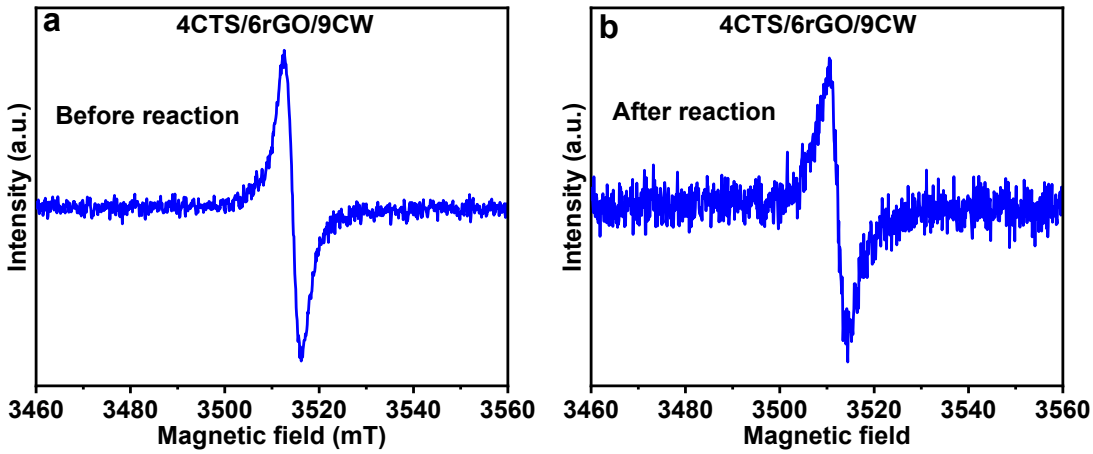

Figure S37. EPR spectra of 4CTS/6rGO/9CW under light conditions, before and after cyclic photocatalytic reaction.

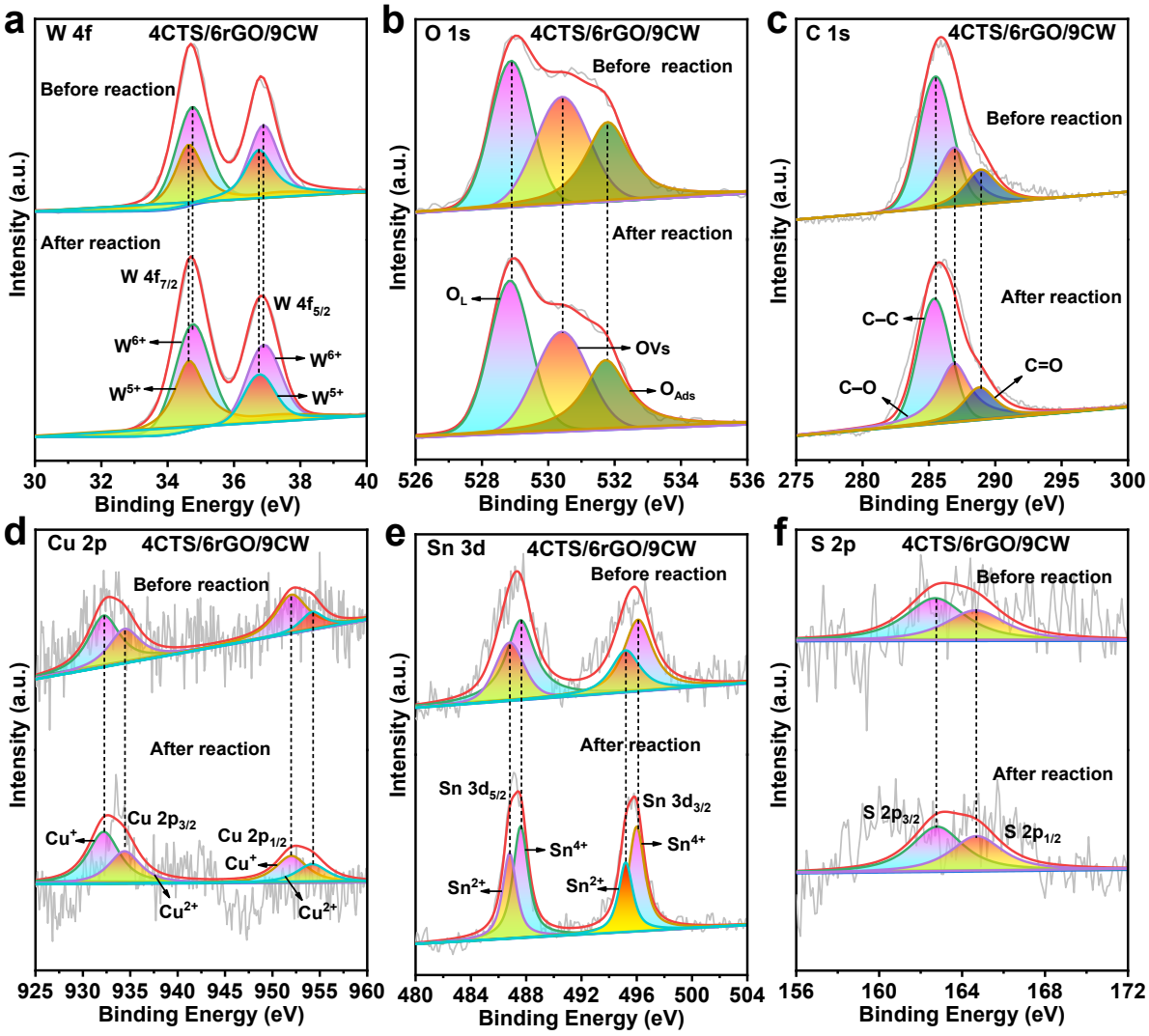

Figure S38. XPS analysis of 4CTS/6rGO/9CW under light conditions, before and after cyclic photocatalytic reaction.

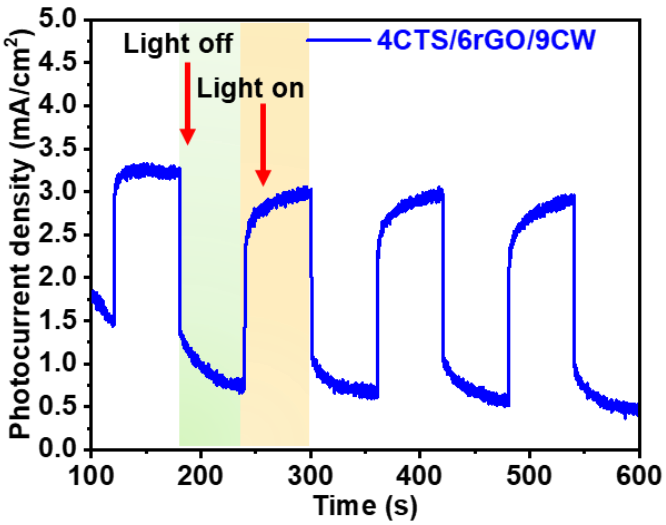

Figure S39. Stability test employing i-t curves of 4CTS/6rGO/9CW.

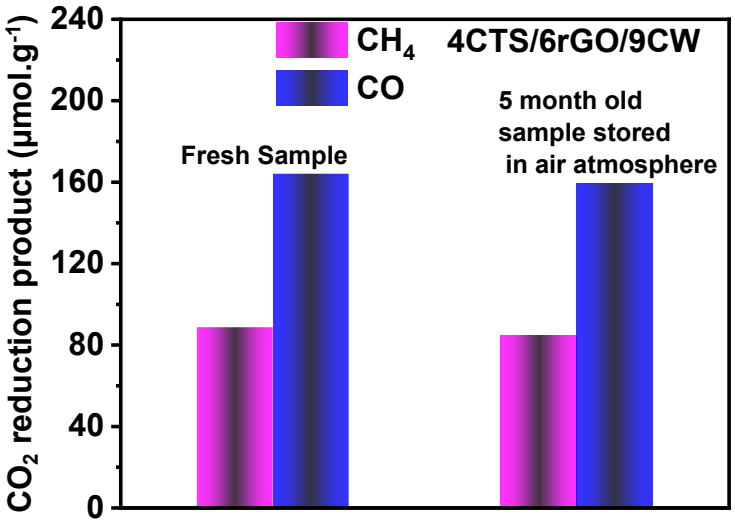

Figure S40. Photocatalytic activity of fresh and old 4CTS/6rGO/9CW sample.

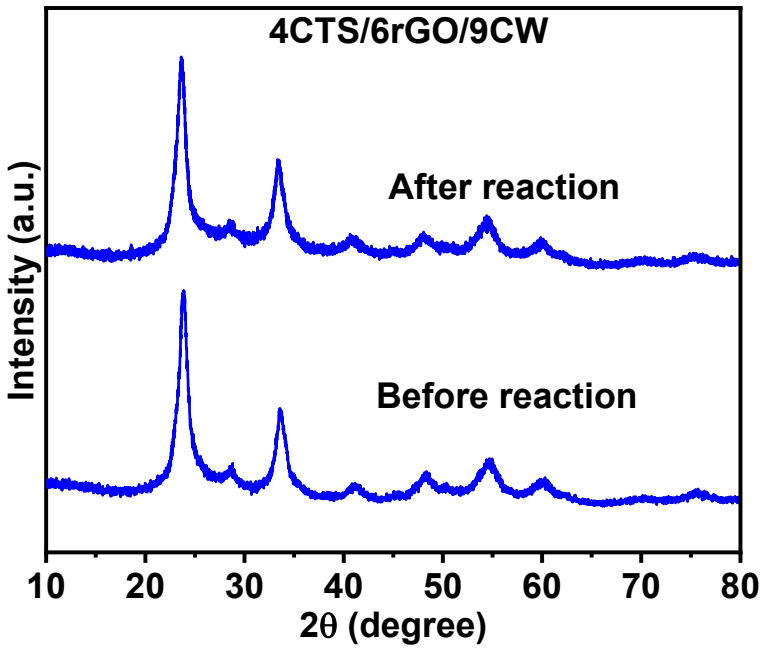

Figure S41. Structural stability employing XRD patterns of 4CTS/6rGO/9CW.

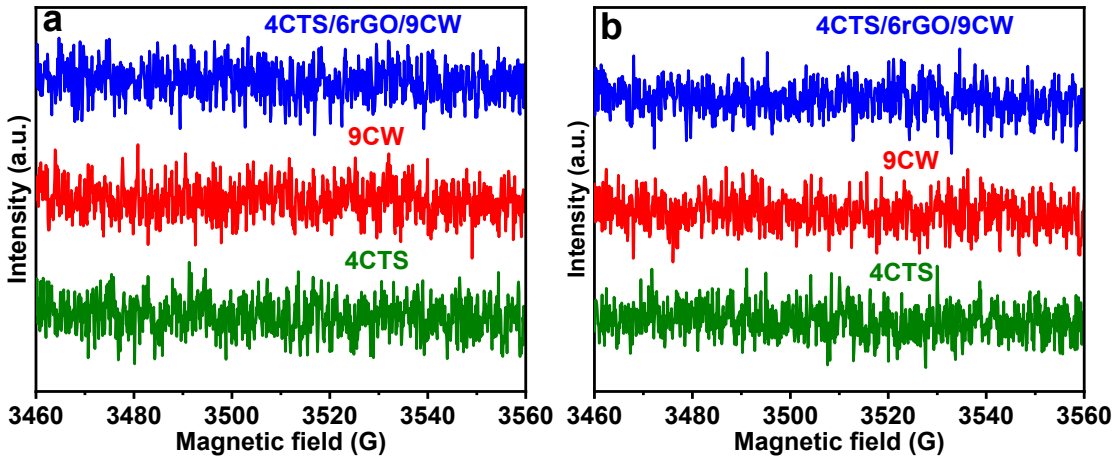

Figure S42. DMPO-trapping EPR spectra for (a)DMPO-•O_2^- and DMPO-•OH radicals in the dark with 4CTS, 9CW, and 4CTS/6rGO/9CW.

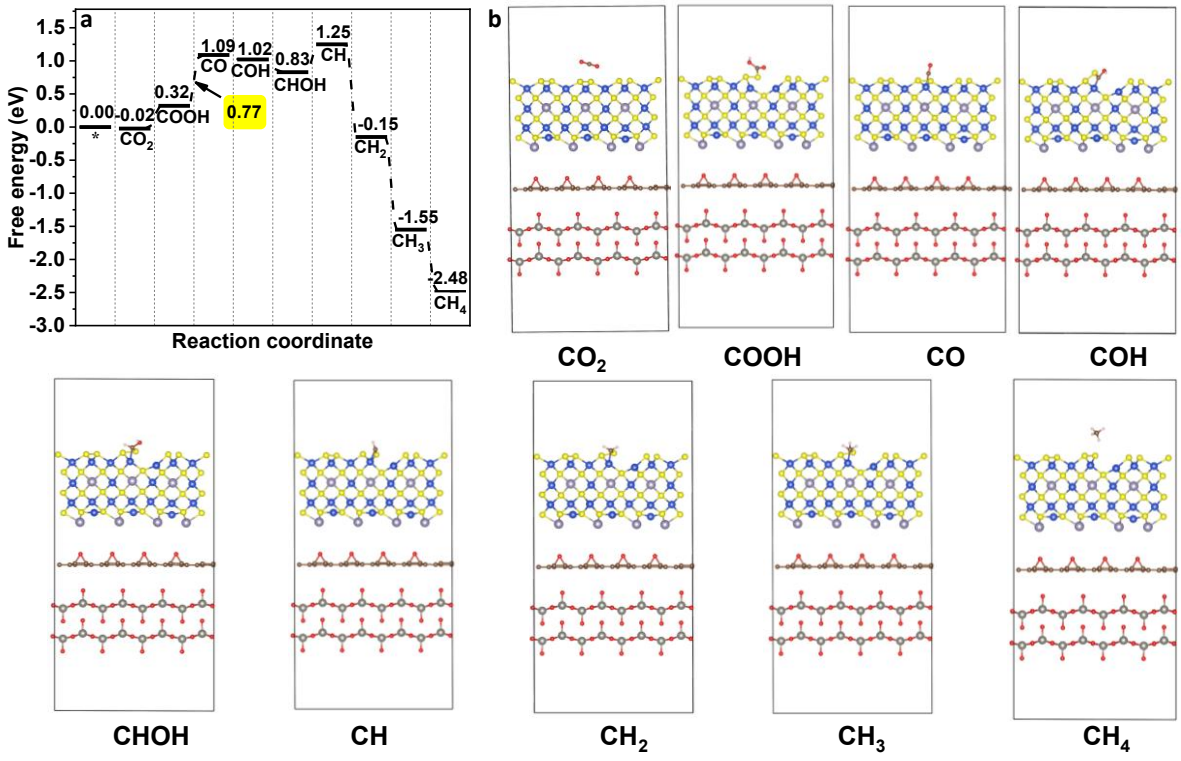

Figure S43. (a-b) free energy diagram of vacancy-free CTS/rGO/WO_3.

Table S1. The photocatalytic performance of CTS/rGO/CW compared with reported literature.

Photocatalyst	Light source	Products (μmol g^{-1} h^{-1})	AQE (%)	References.
CTS/rGO/CW S-scheme heterojunction	Visible light	CO, 164.28 CH_4, 88.79	2.05 at 420 nm	This work
WO_3/Vs-$ZnIn_2S_4$ S-scheme heterojunction	Visible light	CO, 34.7 CH_4, 13.7	-	[1]
$FAPbBr_3$/Bi_2WO_6 Z-scheme heterojunction	150 W Xe lamp with an AM 1.5G filter	CO, 149	1.2 at 400 nm	[2]

Bi-CTS/$BiOBr_{(30)}$ S-scheme heterojunction	300 W xenon lamp	CO, 46.4	-	[3]
OVs-BiOCl / ns-CN Z-scheme heterojunction	300 W xenon lamp	CO, 45.33 CH_4, 0.27	-	[4]
CoPC/P-WS_2 Z-scheme heterojunction	300 W xenon lamp	CO, 28.1 CH_4, 7.3	2.045 at 420 nm	[5]
g-C_3N_4/CDs-WO_3 Z-scheme heterojunction	300 W xenon lamp	CO, 31.04	0.38 at 365 nm	[6]
COF/QDS S-scheme heterojunction	300 W xenon lamp	CO, 41.2 CH_4, 13.7	0.0846 at 420 nm	[7]
WO_3/ZIS S-scheme heterojunction	300 W xenon lamp	CO, 44.61	1.83 at 420 nm	[8]
α-Fe $_2O_3$/g-C_3N_4 Z-scheme heterojunction	300 W xenon lamp	CO, 3.3 CH_4, 30.6	1.98 at 380 nm	[9]

Supplementary note S1:

Initially, CTS and WO_3 were synthesized separately, both in their vacancy-rich and vacancy-free forms. Subsequently, carbon-doped WO_3 samples (zCW, z = 3–12 wt%) were fabricated via a two-step hydrothermal route, with 9CW identified as the optimal composition. CTS was prepared by the simple solvothermal method. Composite materials comprising yrGO-9CW (y = 3–9 wt%) and xCTS/9CW (x = 2–6 wt%) were then prepared through a wet chemical method. To promote charge transfer and enhance CO_2 reduction activity, rGO was integrated as a conductive bridge, [10–12] forming xCTS/rGO/CW heterojunctions. For comparison, vacancy-free CTS/WO_3 and

CTS/rGO/WO_3 heterostructures were also synthesized using identical mass ratios. Detailed synthetic procedures are provided in the Supporting Information (Section 2.1).

Supplementary note S2:

X-ray diffraction (XRD) was employed to investigate the structural evolution across all synthesized materials, including CTS with and without S vacancies, rGO **(Figure S6 and S7)**, bulk WO_3 and carbon-doped WO_3 (zCW, z = 3–12 wt%), 9CW and rGO-modified 9CW (yrGO/9CW, y = 3–9 wt%), and CTS-based composites (xCTS/9CW and xCTS/6rGO/9CW, x = 2–6 wt%) **(Figure S8-S11)**. The diffraction peaks of pristine WO_3 match well with the orthorhombic phase (JCPDS No. 96-210-7313), [13] with prominent reflections at 2θ = 22.92°, 23.48°, 24.52°, and others, corresponding to planes such as (002), (200), and (020). The 9CW sample retains this orthorhombic structure, indicating that carbon doping does not disrupt the host WO_3 lattice. [14] Integration of rGO into 9CW (specifically at 6 wt%) yields a distinct diffraction signal at 2θ = 13.86°, corresponding to partially reduced graphene domains. This, along with a slight sharpening of WO_3-related peaks, indicates the successful incorporation of rGO and improved structural ordering. Further combination with CTS (optimized at 4 wt%) results in sharper reflections for 4CTS/9CW, suggesting enhanced crystallinity driven by defect-rich CTS. Upon introduction of rGO as a conductive bridge in 4CTS/6rGO/9CW, the diffraction peaks exhibit slight intensity suppression alongside sharper profiles, indicative of strong interfacial coupling and suggesting may be structural integrity of the heterojunction **Figure S12**. In contrast, vacancy-free control samples (CTS/WO_3 and CTS/rGO/WO_3, **Figure S13-S14**) exhibit broader peaks and less structural modulation, underscoring the importance of dual-vacancy engineering and rGO mediation in tuning the crystal structure and interfacial quality.

Crystal defects cause the regular arrangement of atoms to be disrupted, which reduces the size of the crystal. Consequently, the Scherrer formula was used to calculate the crystallite sizes of each of the four catalysts. The crystal size of 4CTS/6rGO/9CW (13.4 nm) was smaller than those of 4CTS/9CW (19.4 nm), 9CW (21.45 nm), and bulk WO_3 (28.22 nm) further supporting the calculated average edge length (13.23 nm) of the cubic morphology of 4CTS/6rGO-9CW heterojunction. Similarly, the Raman spectra of all the prepared samples are also displayed in **Figure S15a-d**. The bulk WO_3 shows defect-free spectra, while 9CW illustrate that the D-band (1364 cm^{-1}) is ascribed to the defects, and the G-band (1588 cm^{-1}) is assigned to the graphitic structure and the decreased peak intensity indicates defects suggesting the presence of OV. Interestingly, coupling 9CW with optimized 6rGO and 4CTS causes a further decrease in peak intensities for 4CTS/6rGO/9CW in comparison to the 4CTS/9CW, suggesting more defects indicating the presence of more S and O vacancies **(Figure S16)**. [5,15] Further comparison of the Raman spectra of defect-free CTS/WO_3 and CTS/rGO/WO_3 **(Figure S17a-b)** without S and O vacancies shows a straight line, indicating no defects and confirming the absence of vacancies. These findings, along with the XRD results, collectively support the amenable structural properties of the synthesized materials.

Supplementary note S3:

The work function, a critical factor influencing electron transfer behavior in heterojunctions, was also investigated. [5] CW exhibits a higher work function (7.09 eV, **Figure S29a**) compared to sulfur-deficient CTS (5.49 eV, **Figure S29b**), indicating that the Fermi level of CW (-5.37 eV) is lower than that of CTS (-2.41 eV). This facilitates electron transfer from CTS to CW. **Figure S29c** illustrates the atomic structure of the CTS/CW heterojunction with S and O vacancies (highlighted

with red and black circles), which are known to cause lattice distortions. Although the figure does not directly show defect states within the bandgap, the presence of these vacancies is associated with localized electronic states. Additionally, as anticipated, due to the redistribution of interfacial charge carriers, a built-in electric field with the direction from CTS to CW via rGO could be formed at the interfaces. Hence, it is speculated that the interfacial electric field would guide the photogenerated electrons from CTS to CW in the dark, and reverse under illumination, aligning with the XPS findings, further supporting the dynamic electronic behavior of the system. To further validate this, the S-scheme charge transfer channel in the CTS/rGO/CW heterojunction is illustrated in **Figure S29d-f**. As shown in **Figure S29d**, CW has a lower Fermi level than CTS.

When CW and CTS are brought into close contact in the dark, electrons spontaneously migrate from CTS to CW until their Fermi levels balance. This migration results in a positively charged interface region near CTS due to electron loss, forming a depletion layer and causing upward band bending in CTS, and a negatively charged interface region near CW due to electron accumulation, resulting in downward band bending in CW **(Figure S29e)**. This charge redistribution creates an internal electric field at the CTS/rGO/CW interface, preventing additional electron transfer from CTS to CW. Under light illumination, both CW and CTS undergo photoexcitation, causing electrons to move from their valence bands (VB) to conduction bands (CB). [6,16]

As shown in **Figure S29f**, the internal electric field and Coulombic interactions cause the photogenerated electrons in the CB of CW to recombine with holes in the VB of CTS. This S-scheme charge transfer pathway not only promotes spatial separation of electron-hole pairs but also eliminates less reactive carriers, maintaining highly reductive electrons in the CB of CTS and highly oxidative holes in the VB of CW. While the holes in the VB of CW oxidize H_2O to produce

hydroxyl radicals (•OH), the accumulating electrons in the CB of CTS react with O_2 to generate superoxide radicals ($•O_2^-$). These reactive species significantly enhance redox processes, effectiveness of the S-scheme heterojunction in photocatalytic applications. The introduction of dual S and O vacancies in CTS and CW, respectively, significantly strengthens this process. SVs in CTS and OVs in CW produce defect states near the Fermi level, aligning with DOS results, which enhance conductivity and charge carrier dynamics. The optical and electrochemical properties of the as-synthesized heterojunctions were systematically investigated to understand the influence of dual vacancies (S and O) and rGO on their performance.

Supplementary note S4:

UV-Vis diffuse reflectance spectroscopy (DRS) was used to examine the optical properties and band structure of the as-constructed heterojunctions **(Figure S30)**. All samples exhibited visible light absorption, with the absorption edges of 4CTS/6rGO/9CW showing a redshift compared to 6rGO-9CW, 9CW, and bulk WO_3, suggesting that the cubic structure 4CTS/6rGO/9CW has better light-harvesting capabilities. [17] As a result, 4CTS/6rGO/9CW exhibited the highest photo response, indicating that the addition of O and S vacancies may improve light absorption capacities that produce more electron-hole pairs and hence improve photocatalytic activity. The corresponding band gap energies (E_g) of bulk WO_3, 9CW, and 4CTS were calculated to be 2.85 eV, 2.69 eV, and 2.06 eV, respectively, using the Tauc formula: $(\alpha h\nu)^2 = A\ (h\nu - E_g)$ **(Figure S31)**. The gradual reduction in band gap from bulk WO_3 to 4CTS underscores the importance of dual O and S vacancies and the incorporation of rGO in tuning the heterojunction's electronic structure. [18]

Supplementary note S5:

At first, bulk WO_3 showed little photocatalytic activity for reducing CO_2, resulting in modest outputs of CH_4 and CO. We thoroughly examined how C loading affected WO_3 in order to improve its performance. A 9 wt% C loading on WO_3 (referred to as 9CW) produced the maximum CO_2 conversion to CO and CH_4, as seen in **Figure S35a**. The decrease in photocatalytic activity that came from exceeding this optimal loading was most likely caused by the self-aggregation of C molecules on the WO_3 surface, which reduced the availability of active sites for CO_2 photoreduction. In order to guarantee a uniform 9 wt% C injection, we employed rGO as a modulator. Different rGO loadings (referred to as yrGO/9CW, where y = 3, 6, and 9 wt %) were tested. As shown in **Figure 35b**, the results showed a progressive increase in photocatalytic activity up to 6 wt % rGO (i.e., 6rGO/9CW), after which a decrease was noted for the 9 wt% loading. This implies that high rGO loading could negate the positive benefits of light absorption by blocking active sites or obstructing light absorption. To further improve the system, we produced a composite of 9CW with different loadings of xCTS (x = 2, 4, and 6 wt%). As seen in **Figure 35c**, the 4 wt % CTS loading (4CTS/9CW) exhibited the maximum photocatalytic activity among these. Because of the synergistic effects of CTS, rGO, and CW, which together improve charge separation, light absorption, and the availability of active sites for CO_2 reduction, the addition of 6 wt% rGO to the 4CTS/9CW composite produced a complete heterojunction (4CTS/6rGO/9CW), which demonstrated a significant improvement in photocatalytic performance, as shown in **Figure 35d**. These results emphasize the significance of optimizing material composition and loading to achieve maximum photocatalytic efficiency for CO_2 conversion.

Supplementary note S6:

Calculation of apparent quantum efficiency for CO_2 Conversion

The calculated quantum efficiency of Bulk WO_3, 4CTS, 9CW, 6rGO/9CW, 4CTS/9CW and 4CTS/6rGO/9CW for CO_2 reduction at λ = 420 nm were measured. The catalyst mixture was irradiated by a 300 W Xe lamp for 8 h. The average incident irradiation was determined to be 2.01 mW/cm^2 by Newport (Oriel instrument USA model 91150V ser. No 391/0118) and the area was 5.5 cm^2. The amount of CH_4 gas produced in 8 h on bulk WO_3, 9CW, 4CTS, 6rGO-9CW, 4CTS/9CW, and 4CTS/6rGO-9CW was 0.07, 0.10, 0.21, 0.12, 0.68 and 0.98 μmol at 420 nm. The amount of CO gas produced in 8 h on bulk WO_3, 9CW, 4CTS, 6rGO/9CW, 4CTS/9CW, and 4CTS/6rGO-9CW was 0.36, 2.19, 2.54, 2.33, 5.23, and 7.56 μmol. All the calculations are given below.

Number of incident photons in 8 h over 5.5 cm^2 area:

Quantum efficiency at 420 nm of bulk WO_3

$$N = \frac{E\lambda}{hc} = \frac{2.01 \times 10^{-3} \times 5.5 \times 420 \times 10^{-9} \times 8 \times 3600}{6.626 \times 10^{-34} \times 3 \times 10^{8}} = 6.73 \times 10^{20}$$

$$\text{QE} = \frac{(2 \times the\ number\ CO) + 8 \times the\ number\ of\ CH_4\ molecules\ produced}{the\ number\ of\ incident\ photons} \times 100\%$$

$$\text{QE}_{\text{Bulk WO3}} = \frac{((2 \times 0.36) + (8 \times 0.07)) \times 10^{-6} \times 6.02 \times 10^{23}}{6.73 \times 10^{20}} \times 100\% = 0.11\%$$

Quantum efficiency at 420 nm of optimized 9CW

$$N = \frac{E\lambda}{hc} = \frac{2.01 \times 10^{-3} \times 5.5 \times 420 \times 10^{-9} \times 8 \times 3600}{6.626 \times 10^{-34} \times 3 \times 10^{8}} = 6.73 \times 10^{20}$$

$$\text{QE} = \frac{(2 \times the\ number\ CO) + 8 \times the\ number\ of\ CH_4\ molecules\ produced}{the\ number\ of\ incident\ photons} \times 100\%$$

$$QE_{9CW}=\frac{((2\times2.19)+(8\times0.10))\times10^{-6}\times 6.02\times 10^{23}}{6.73\times10^{20}}\times 100\% = 0.46\%$$

Quantum efficiency at 420 nm of 4CTS

$$N=\frac{E\lambda}{hc}=\frac{2.01\ \times\ 10^{-3}\times 5.5\ \times 420\ \times\ 10^{-9}\ \times 8\times 3600}{6.626\times\ 10^{-34}\ \times 3\ \times\ 10^{8}}\ =6.73\times10^{20}$$

$$QE=\frac{(2\times the\ number\ CO)+\ 8\times\ the\ number\ of\ CH_4\ molecules\ produced}{the\ number\ of\ incident\ photons}\times 100\%$$

$$QE_{4CTS}=\frac{((2\times2.54)+(8\times0.21))\times10^{-6}\times 6.02\times 10^{23}}{6.73\times10^{20}}\times 100\% = 0.60\%$$

Quantum efficiency at 420 nm of 6rGO-9CW

$$N=\frac{E\lambda}{hc}=\frac{2.01\ \times\ 10^{-3}\times 5.5\ \times 420\ \times\ 10^{-9}\ \times 8\times 3600}{6.626\times\ 10^{-34}\ \times 3\ \times\ 10^{8}}\ =6.73\times10^{20}$$

$$QE=\frac{(2\times the\ number\ CO)+\ 8\times\ the\ number\ of\ CH_4\ molecules\ produced}{the\ number\ of\ incident\ photons}\times 100\%$$

$$QE_{6rGO/9CW}=\frac{((2\times2.33)+(8\times0.12))\times10^{-6}\times 6.02\times 10^{23}}{6.73\times10^{20}}\times 100\% = 0.50\%$$

Quantum efficiency at 420 nm of 4CTS/9CW composite

$$N=\frac{E\lambda}{hc}=\frac{2.01\ \times\ 10^{-3}\times 5.5\ \times 420\ \times\ 10^{-9}\ \times 8\times 3600}{6.626\times\ 10^{-34}\ \times 3\ \times\ 10^{8}}\ =6.73\times10^{20}$$

$$QE=\frac{(2\times the\ number\ CO)+\ 8\times\ the\ number\ of\ CH_4\ molecules\ produced}{the\ number\ of\ incident\ photons}\times 100\%$$

$$QE_{4CTS/9CW}=\frac{((2\times5.23)+(8\times0.68))\times10^{-6}\times 6.02\times 10^{23}}{6.73\times10^{20}}\times 100\% = 1.42\%$$

Quantum efficiency at 420 nm of 4CTS/6rGO-9CW heterojunction

$$N = \frac{E\lambda}{hc} = \frac{2.01 \times 10^{-3} \times 5.5 \times 420 \times 10^{-9} \times 8 \times 3600}{6.626 \times 10^{-34} \times 3 \times 10^{8}} = 6.73 \times 10^{20}$$

$$\text{QE} = \frac{(2 \times the\ number\ CO) + 8 \times the\ number\ of\ CH_4\ molecules\ produced}{the\ number\ of\ incident\ photons} \times 100\%$$

$$\text{QE}_{4CTS/6rGO/9CW} = \frac{((2 \times 7.56) + (8 \times 0.98)) \times 10^{-6} \times 6.02 \times 10^{23}}{6.73 \times 10^{20}} \times 100\% = 2.05\%$$

Calculation of AQE for CO

The number of incident photons in 8h over 5.5 cm^2 area:

$$QE = \frac{(2 \times the\ number\ co)}{the\ number\ of\ incident\ photons} \times 100\%$$

Quantum efficiency at 420 nm

$$N = \frac{E\lambda}{hc} = \frac{2.01 \times 10^{-3} \times 5.5 \times 420 \times 10^{-9} \times 8 \times 3600}{6.626 \times 10^{-34} \times 3 \times 10^{8}} = 6.73 \times 10^{20}$$

$$\text{QE}_{\text{Bulk WO3}} = \frac{(2 \times 0.36) \times 10^{-6} \times 6.02 \times 10^{23}}{6.73 \times 10^{20}} \times 100\% = 0.06\%$$

$$\text{QE}_{9CW} = \frac{(2 \times 2.19) \times 10^{-6} \times 6.02 \times 10^{23}}{6.73 \times 10^{20}} \times 100\% = 0.39\%$$

$$\text{QE}_{4CTS} = \frac{(2 \times 2.54) \times 10^{-6} \times 6.02 \times 10^{23}}{6.73 \times 10^{20}} \times 100\% = 0.45\%$$

$$\text{QE}_{6rGO/9CW} = \frac{(2 \times 2.33) \times 10^{-6} \times 6.02 \times 10^{23}}{6.73 \times 10^{20}} \times 100\% = 0.42\%$$

$$QE_{4CTS/9CW} = \frac{(2\times5.23)\times10^{-6}\times 6.02\times 10^{23}}{6.73\times10^{20}} \times 100\% = 0.93\%$$

$$QE_{4CTS/6rGO/9CW} = \frac{(2\times7.56)\times10^{-6}\times 6.02\times 10^{23}}{6.73\times10^{20}} \times 100\% = 1.35\%$$

Calculation of AQE for CH_4

The number of incident photons in 8h over 5.5 cm^2 area:

$$QE = \frac{8\times the\ number\ of\ CH_4\ molecules\ produced}{the\ number\ of\ incident\ photons} \times 100\%$$

Quantum efficiency at 420 nm

$$N = \frac{E\lambda}{hc} = \frac{2.01\ \times\ 10^{-3} \times 5.5\ \times 420\ \times\ 10^{-9}\ \times 8 \times 3600}{6.626 \times\ 10^{-34}\ \times 3\ \times\ 10^{8}}\ = 6.73 \times 10^{20}$$

$$QE_{Bulk\ WO3} = \frac{(8\times0.07)\times10^{-6}\times 6.02\times 10^{23}}{6.73\times10^{20}} \times 100\% = 0.05\%$$

$$QE_{9CW} = \frac{(8\times0.10)\times10^{-6}\times 6.02\times 10^{23}}{6.73\times10^{20}} \times 100\% = 0.07\%$$

$$QE_{4CTS} = \frac{(8\times0.21)\times10^{-6}\times 6.02\times 10^{23}}{6.73\times10^{20}} \times 100\% = 0.15\%$$

$$QE_{6rGO/9CW} = \frac{(8\times0.12)\times10^{-6}\times 6.02\times 10^{23}}{6.73\times10^{20}} \times 100\% = 0.08\%$$

$$QE_{4CTS/9CW} = \frac{(8\times0.68)\times10^{-6}\times 6.02\times 10^{23}}{6.73\times10^{20}} \times 100\% = 0.49\%$$

$$QE_{4CTS/rGO/9CW} = \frac{(8\times0.98)\times10^{-6}\times 6.02\times 10^{23}}{6.73\times10^{20}} \times 100\% = 0.70\%$$

Supplementary note S7:

The carbon dioxide reduction reaction (CO_2RR) to methane (CH_4) is a complex, multi-step process involving a series of proton-coupled electron transfer reactions. It begins with the adsorption and activation of CO_2 molecules on the catalyst surface, a crucial step that initiates the conversion. Upon adsorption, CO_2 interacts with surface metal atoms, typically through its oxygen atoms, forming weak bonds that destabilize the molecule and prepare it for further reduction. Following activation, CO_2 undergoes stepwise hydrogenation to generate key reaction intermediates. One of the earliest intermediates is formic acid (*COOH), which forms via the first hydrogenation step. This is followed by its reduction to carbon monoxide (*CO), a pivotal species in the CH_4 production pathway. The cleavage of the C=O bond at this stage liberates an adsorbed oxygen atom (*O), while the *CO intermediate continues through successive hydrogenation steps to yield methanol-like intermediates (e.g., *CH_3OH), ultimately forming a methyl species (*CH_3). This methyl group, upon further hydrogenation, generates methane, which then desorbs from the catalyst surface to complete the transformation. Each of these reaction steps is governed by its respective energy profile. While some steps are exothermic and proceed readily, others are endothermic, requiring higher activation energies and often serving as rate-determining steps. The catalyst plays a vital role in lowering these energy barriers, enhancing both the kinetics and the selectivity of the CO_2RR. To gain mechanistic insights into the energetics of this transformation,

density functional theory (DFT) calculations were conducted to evaluate the free energy profile for CO_2 reduction to CH_4 over a vacancy-free CTS/rGO/WO_3 catalyst.

References

1 X. Zhang, W. Ni, X. Yue, Z. Wang, Z. Zhang, K. Wang, W. Dai and X. Fu, *J. Colloid Interface Sci.*, 2025, **678**, 233–245.

2 H. Huang, J. Zhao, Y. Du, C. Zhou, M. Zhang, Z. Wang, Y. Weng, J. Long, J. Hofkens, J. A. Steele and M. B. J. Roeffaers, *ACS Nano*, 2020, **14**, 16689–16697.

3 Z. Li, Y. Rong, J. Liang, Z. Li, J. Wei, J. Li, S. Zhang, T. Liang, Z. Yu and Y. Hou, *J. Environ. Chem. Eng.*, 2022, **10**, 108819.

4 S. Cheng, Z. Sun, K. H. Lim, A. A. Wibowo, T. Zhang, T. Du, L. Liu, H. T. Nguyen, G. K. Li, Z. Yin and S. Kawi, *ACS Catal.*, 2023, **13**, 7221–7229.

5 P. M. Ismail, S. Ali, S. Ali, J. Li, M. Liu, D. Yan, F. Raziq, F. Wahid, G. Li, S. Yuan, X. Wu, J. Yi, J. S. Chen, Q. Wang, L. Zhong, Y. Yang, P. Xia and L. Qiao, *Adv. Mater.*, 2023, **35**, 2303047.

6 X. Kong, J. Fan, B. Feng, J. Li, G. Yang and C. Xue, *Chem. Eng. J.*, 2023, **476**, 146774.

7 Y. He, P. Hu, J. Zhang, G. Liang, J. Yu and F. Xu, *ACS Catal.*, 2024, **14**, 1951–1961.

8 A. Xu, Y. Zhang, H. Fan, X. Liu, F. Wang, X. Qu, L. Yang, X. Li, J. Cao and M. Wei, *ACS Appl. Nano Mater.*, 2024, **7**, 3488–3498.

9 Y. Gao, M. Zhang, Y. Jin, Y. Mao, W. Wang and Z. Song, *ACS Catal.*, 2024, **14**, 10746–10759.

10 F. Raziq, M. Z. Rahman, S. Ali, R. Ali, S. Ali, A. Zada, X. Wu, J. Gascon, Q. Wang and L. Qiao, *Chem. Eng. J.*, 2024, **479**, 147712.

11 Y. Baghdadi, M. Daboczi, F. Temerov, M. Yang, J. Cui and S. Eslava, *J. Mater. Chem. A*, 2024, **12**, 16383–16395.

12 Z. Yin, J. Zhu, Q. He, X. Cao, C. Tan, H. Chen, Q. Yan and H. Zhang, *Adv. Energy Mater.*, 2014, **4**, 1300574.

13 M. R. Kamal, M. Z. Rahman, A. Aligayev, M. Liu, L. Zhong, P. Xia, Y. Li, Y. Ruan, X. Xiang, P. M. Ismail, Q. Alam, A. Ismail, M. Zahid, X. Wu, A. N. Alodhayb, Q. Huang, R. W. Khan, F. Raziq, S. Ali and L. Qiao, *Sep. Purif. Technol.*, 2025, **370**, 133187.

14 B. Lei, W. Cui, P. Chen, L. Chen, J. Li and F. Dong, *ACS Catal.*, 2022, **12**, 9670–9678.

15 H. Liu, Z. Chen, Z. Jin, Y. Su and Y. Wang, *Dalt. Trans.*, 2014, **43**, 7491–7498.

16 X. Han, B. Lu, X. Huang, C. Liu, S. Chen, J. Chen, Z. Zeng, S. Deng and J. Wang, *Appl. Catal. B Environ.*, 2022, **316**, 121587.

17 W. Gao, G. Li, Q. Wang, L. Zhang, K. Wang, S. Pang, G. Zhang, L. Lv, X. Liu, W. Gao, L. Sun, Y. Xia, Z. Ren and P. Wang, *Chem. Eng. J.*, 2023, **464**, 142694.

18 R. Zhang, R. Liu, Z. Ding, J. Ma, T. Wang, D. Zhang, J. Liu, P. Cai and X. Pu, *J. Colloid Interface Sci.*, 2025, **682**, 568–577.